RESEARCH ARTICLE

WILEY

Transported snapshot model order reduction approach for parametric, steady-state fluid flows containing parameter-dependent shocks

Nirmal J. Nair | Maciej Balajewicz

Department of Aerospace Engineering, University of Illinois at Urbana–Champaign, Urbana, Illinois

Correspondence
Nirmal J. Nair, Department of Aerospace Engineering, University of Illinois at Urbana–Champaign, Urbana, IL 61801.
Email: njn2@illinois.edu

Summary

A new model order reduction approach is proposed for parametric steady-state nonlinear fluid flows characterized by shocks and discontinuities whose spatial locations and orientations are strongly parameter dependent. In this method, solutions in the predictive regime are approximated using a linear superposition of parameter-dependent basis. The sought-after parametric reduced bases are obtained by transporting the snapshots in a spatially and parametrically dependent transport field. Key to the proposed approach is the observation that the transport fields are typically smooth and continuous, despite the solution themselves not being so. As a result, the transport fields can be accurately expressed using a low-order polynomial expansion. Similar to traditional projection-based model order reduction approaches, the proposed method is formulated mathematically as a residual minimization problem for the generalized coordinates. The proposed approach is also integrated with well-known hyper-reduction strategies to obtain significant computational speedups. The method is successfully applied to the reduction of a parametric one-dimensional flow in a converging-diverging nozzle, a parametric two-dimensional supersonic flow over a forward-facing step, and a parametric two-dimensional jet diffusion flame in a combustor.

KEYWORDS

hyperbolic PDE, parametric model order reduction, shock, steady-state residual

1 | INTRODUCTION

Computational models of high-dimensional systems arise in a rich variety of engineering and scientific contexts. Computational fluid dynamics (CFD), for example, has become an indispensable tool for many engineering applications across a wide range of industries. Unfortunately, high-fidelity CFD simulations are often so computationally prohibitive that they cannot be used as often as needed or used only in special circumstances rather than routinely. Consequently, the impact of CFD on parametric and time-critical applications, such as design, optimization, and control, has not yet been fully realized. Model order reduction (MOR) is a serious contender for bridging this gap.

Most existing MOR approaches are based on projection. In projection-based MOR, the state variables are approximated in a low-dimensional subspace. Over the years, a number of approaches for calculating a reduced-order basis (ROB) have been developed, eg, proper orthogonal decomposition (POD),[1,2] dynamic mode decomposition,[3,4] balanced POD,[5,6] balanced truncation,[7,8] and the reduced-basis method.[9,10]

For a reduced-order model (ROM) to be truly useful, it must be capable of generating accurate predictions for parameter values that are different from those sampled for the purpose of constructing an ROB. Generating ROBs and ROMs that are robust to parameter variations is an active area of research.[11] The choice of parameter sample points is critical to any method used to generate the basis. For problems with smaller number of parameters, a simple approach like random sampling using the Latin hypercube method is often sufficient.[12] For problems with large number of parameters, more sophisticated sampling methods are usually required. In the standard greedy sampling approach,[13-16] the sample points are chosen one by one in an adaptive manner. At every iteration, the goal is to find the parameter value for which the error between the ROM and the full-order model (FOM) is largest. The FOM is sampled at this point, and the new information is used to generate a new reduced basis.

Another critical issue involves the choice between a global or a local basis. Although the global basis has been shown to perform adequately for many applications,[17-20] particularly challenging problems often necessitate the use of multiple local reduced bases.[21,22] In these cases, several local bases are constructed and linked to particular regions in the parameter or state space.[23-25] The price of this additional flexibility is the switching algorithm required to switch between the local bases. Finally, to improve the ROM performance in predictive regimes, it is also possible to interpolate the bases or the ROM matrices.[26-28]

Achieving parametric robustness is particularly challenging when the sought-after solutions contain sharp gradients, discontinuities, or shocks. These situations arise in a wide range of important engineering applications, for example, high-speed fluid flows,[29,30] multiphase flows with evolving material interfaces,[31] computational finance,[32] and the structural contact problem with evolving contact regions.[33]

Over the years, a large variety of discontinuity-aware MOR techniques have been developed. In the first class of such methods, the problem of modeling discontinuities is avoided entirely by exploiting the symmetry and transport reversal properties of certain hyperbolic partial differential equations (PDEs).[34-36] Other methods involve decomposition into global and advection modes governed by optimal mass transfer[37] or a more direct modeling of discontinuities using basis splitting[38] or snapshot transformation.[39-41] For unsteady solutions with shocks, accurate low-rank solutions can be obtained using a Lagrangian framework,[42] where both the position and state of Lagrangian particle variables are approximated by their respective ROBs. Other methods decompose the solution into a variable separable form consisting of an evolution term to capture moving shocks and a diffusion term to capture the changing shapes.[43] Finally, other methods avoid the problem of modeling discontinuities by domain decomposition, where direct numerical simulation or reconstruction methods are used in regions containing the discontinuities.[44-46]

In this paper, we outline our new proposed approach for parametric model reduction of solutions containing moving shocks and discontinuities. In our proposed approach, solutions in the predictive regime are approximated using a parameter-dependent basis. Snapshots are transported in a spatially and parametrically dependent transport field to yield transported snapshots. These transported snapshots form the parameter-dependent basis for the proposed MOR. Key to our proposed approach is the observation that the transport fields are smooth and, thus, can be themselves approximated using a low-order expansion. Our method may be interpreted as a data-driven generalization of the previous works of Rowley and Marsden[36] and Iollo and Lombardi.[37]

The remainder of this paper is organized as follows. In Section 2, the problem of interest and the traditional projection-based MOR approach are recapitulated. The proposed methodology for approximating unsampled solutions via transported snapshots for one-dimensional (1D) parameter variational problems is detailed in Section 3, and its extension to multidimensions is detailed in Section 4. The details for the numerical implementation of our new approach in the discrete framework are provided in Section 5. In Section 6, the proposed approach is integrated with a hyper-reduction algorithm. In Section 7, the novelty of the proposed approach is compared with similar existing methods in the literature. In Section 8, the performance of the proposed method is evaluated on several simple but representative fluid flow models. Limitations of the proposed approach are discussed in Section 9. Finally, in Section 10, conclusions are offered, and prospects for future work are summarized.

2 | PROBLEM STATEMENT

2.1 | Full-order model

We consider FOMs consisting of hyperbolic or convection-dominated parabolic PDEs such as the Euler or high-Reynolds-number Navier-Stokes equations, ie,

$$\frac{\partial \boldsymbol{u}}{\partial t} + \boldsymbol{f}(\boldsymbol{u}, \boldsymbol{x}; \boldsymbol{\mu}) = \boldsymbol{0}, \tag{1}$$

where the state variable $\boldsymbol{u} = \boldsymbol{u}(\boldsymbol{x}, t; \boldsymbol{\mu})$ depends on space $\boldsymbol{x} \in \Omega$, with Ω being the flow domain, time $t \in [0, t_{\max}]$, and a vector of N_d parameters $\boldsymbol{\mu} \in \mathcal{D} \subset \mathbb{R}^{N_d}$ (where $\mathcal{D}$ is a bounded domain). Moreover, $\boldsymbol{f}$ is the nonlinear function that contains the convective and diffusive fluxes.

The steady-state equation for this system can be written as

$$\boldsymbol{R}(\boldsymbol{u}; \boldsymbol{\mu}) := \boldsymbol{f}(\boldsymbol{u}, \boldsymbol{x}; \boldsymbol{\mu}) = \boldsymbol{0}, \tag{2}$$

where $\boldsymbol{R}(\boldsymbol{u}; \boldsymbol{\mu})$ is the steady-state residual. To obtain steady-state solutions, Equation (2) can be discretized in space by a standard finite difference/volume/element method. The resulting set of equations can be solved directly by an iterative method, or a time-stepping method can be used to advance the semidiscretized form of unsteady Equation (1) to a steady state.

2.2 | Traditional nonlinear model reduction

In traditional projection-based MOR, the state variable $\boldsymbol{u}(\boldsymbol{x}; \boldsymbol{\mu})$ is approximated in a global low-dimensional trial subspace as follows:

$$\boldsymbol{u}(\boldsymbol{x}; \boldsymbol{\mu}) \approx \boldsymbol{u}_r = \sum_{n=1}^{N_k} \boldsymbol{u}_n(\boldsymbol{x}) a_n(\boldsymbol{\mu}), \tag{3}$$

where $\boldsymbol{u}_n$ is the basis of this subspace, N_k is the number of bases, and $\boldsymbol{a}(\boldsymbol{\mu}) \in \mathbb{R}^{N_k}$ denotes the generalized coordinates in this basis. Substituting the approximation (3) into the residual equation (2) yields $\boldsymbol{R}(\boldsymbol{u}_r; \boldsymbol{\mu}) = \boldsymbol{0}$. Consequently, the generalized coordinates are chosen to minimize the residual of the Galerkin expansion, ie,

$$(\boldsymbol{v}_n, \boldsymbol{R}(\boldsymbol{u}_r; \boldsymbol{\mu}))_\Omega, \tag{4}$$

where $\boldsymbol{v}_n$ is the basis of the test subspace, and the inner product is defined as

$$(\boldsymbol{u}, \boldsymbol{v})_\Omega := \int_\Omega \boldsymbol{u}.\boldsymbol{v} d\boldsymbol{x}. \tag{5}$$

If the test basis $\boldsymbol{v}_n \neq \boldsymbol{u}_n$, then the projection in Equation (4) is called the Petrov-Galerkin projection with the specific case $\boldsymbol{v}_n = \boldsymbol{J}\boldsymbol{u}_n$ known as the least squares Petrov-Galerkin (LSPG) projection, where $\boldsymbol{J} = \partial \boldsymbol{R}/\partial \boldsymbol{a}$ denotes the Jacobian of the residual. For nonlinear, non–self-adjoining problems such as those represented in this case by the set of ODEs, this approach is more robust than a Galerkin projection, where $\boldsymbol{v}_n = \boldsymbol{u}_n$.

Solving the minimization problem in Equation (4) requires the evaluation of the residual of the governing equations of the high-dimensional state variables. The complexity of this computation scales with the size of the FOM. Therefore, while MOR approximates the FOM in a low-dimensional subspace, part of the computational cost still scales with the size of the FOM. For general nonlinear systems, an additional level of approximation—sometimes called "hyper-reduction" such as the discrete empirical interpolation method (DEIM),[47] the Gauss-Newton with approximated tensors method,[48] and the energy-conserving sampling and weighting (ECSW) method[49]—is therefore required.

2.3 | Drawbacks

In data-driven projection-based MOR, the ROBs are usually constructed off-line by collecting solution snapshots $\boldsymbol{u}(\boldsymbol{x}; \boldsymbol{\mu}_s)$ of problem (2) for different instances $\boldsymbol{\mu}_s$ for $s = 1, \ldots, N_s$, of the parameter vector $\boldsymbol{\mu}$. The ROBs are then formed by selecting a small subset of the snapshots or via compression using, for example, POD.

For an ROM to be useful, however, it must be capable of providing solutions at parameters $\boldsymbol{\mu}^*$ not sampled during the off-line basis construction phase, $\boldsymbol{\mu}^* \neq \boldsymbol{\mu}_s$. Although parameter robustness is an active area of research, it is particularly challenging when the sought-after solutions contain discontinuities or sharp gradients whose spatial orientations are strongly parameter dependent.

To illustrate, consider the simple problem of a quasi-1D supersonic flow in a converging-diverging nozzle governed by 1D Euler equations. The area profile, $A(x)$, of the nozzle is parabolic with equal inlet and outlet areas, $A(0) = A(L)$, and the throat is located at $L/2$, where L is the length of the nozzle. For this problem, the throat area $\mu = A(L/2)$ is the varying parameter of interest. Refer to Section 8.1.1 for the details of this problem. Four snapshots at parameters $\mu_s = [0.5, 0.875, 1.25, 1.625]$ are generated, and the corresponding steady-state density solutions are shown in Figure 1A.
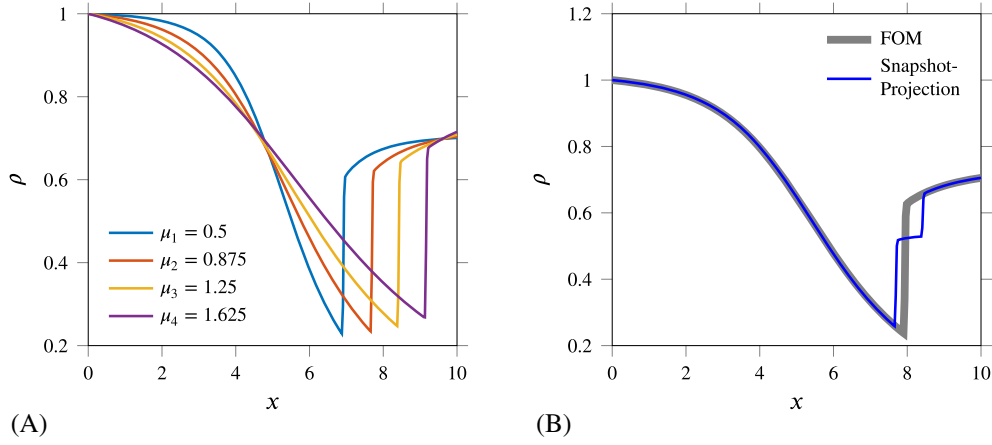
FIGURE 1 Steady-state solutions at μ_s and an optimally constructed solution at μ^*. A, Steady-state density solution ρ for various throat area parameters μ_s; B, Comparison of the optimally constructed solution by Snapshot-Projection with a full-order model (FOM) at $\mu^* = 1.0$

The optimal construction of a new solution at an unsampled parameter μ^* is given by a superposition of the sampled snapshots, ie,

$$\boldsymbol{u}_r(\boldsymbol{x}; \mu^*) = \sum_{s=1}^{N_s} \boldsymbol{u}(\boldsymbol{x}; \mu_s) a_n(\mu^*), \qquad (6)$$

where the coordinates, $\boldsymbol{a}(\mu^*)$, are obtained by projecting the FOM solution onto the snapshots. The FOM and optimally constructed solutions at $\mu^* = 1.0$ ($\mu_2 < \mu^* < \mu_3$) are plotted in Figure 1B. It can be observed that the optimally constructed solution is dominated by a staircase shock–type error. Moreover, the optimal coordinates are $\boldsymbol{a}(\mu^*) = [-0.006, 0.333, 0.688, -0.016]$, where the coordinates corresponding to the first and fourth snapshots (a_1 and a_4, respectively) are significantly lower than the coordinates corresponding to the second and third snapshots (a_2 and a_3, respectively). This implies that the optimal construction is significantly dominated by local nearby snapshots.

This toy problem demonstrates that (i) optimal constructions of solutions characterized by parameter-dependent shocks and discontinuities are typically local and sparse in the sense that only two bases were required for the construction and that (ii) the optimal construction provides a "staircase" approximation of the true solution. In summary, neither global nor local reduced basis can be expected to yield efficient approximations in the predictive regime of solutions characterized by shocks, discontinuities, and sharp gradients whose physical locations and orientations are parameter dependent.

3 | TRANSPORTED SNAPSHOT MODEL ORDER REDUCTION

In this paper, we introduce and summarize our new MOR approach for parametric and steady nonlinear fluid flows characterized by moving shocks, discontinuities, and sharp gradients. In this section, the proposed method is initially developed and detailed for 1D parameter variational problems, whereas the extension of this method for multidimensional parameter variations is later detailed in Section 4.

Our proposed approach is motivated by the observation that for many problems of interest, such as the motivational problem illustrated in Figure 1A, snapshots local in the parameter space are transported in physical space. More precisely, if $\boldsymbol{u}(\boldsymbol{x}; \mu_j)$ and $\boldsymbol{u}(\boldsymbol{x}; \mu_{j+k})$ are the sampled solutions of the FOM at parameters μ_j and μ_{j+k}, respectively, then there exists continuous and smooth transport field $\boldsymbol{c}_j(\boldsymbol{x}, \Delta\mu)$ such that

$$\boldsymbol{u}(\boldsymbol{x}; \mu_{j+k}) \approx \boldsymbol{u}\left(\boldsymbol{x} + \boldsymbol{c}_j(\boldsymbol{x}, \Delta\mu); \mu_j\right), \qquad (7)$$

where $\Delta\mu = \mu_{j+k} - \mu_j$ is the parameter variation between the original snapshot $\boldsymbol{u}(\boldsymbol{x}, \mu_j)$ and the target snapshot $\boldsymbol{u}(\boldsymbol{x}, \mu_{j+k})$.

Approximating the solution at an *unsampled* parameter $\mu^* \neq \mu_s$, for $s = 1, \ldots, N_s$, proceeds similarly to the traditional projection-based MOR. More specifically, we assume that the solution can be approximated as a linear superposition of parameter-dependent basis functions, ie,

$$\boldsymbol{u}(\boldsymbol{x}; \mu^*) \approx \boldsymbol{u}_r = \sum_{n=1}^{N_k} \boldsymbol{u}_n(\boldsymbol{x}; \mu^*) a_n(\mu^*), \qquad (8)$$

where the reduced-basis functions $\boldsymbol{u}_n$ correspond to the *transported* local snapshots, ie,

$$\boldsymbol{u}_n = \boldsymbol{u}\left(\boldsymbol{x} + \boldsymbol{c}_{k_n}(\boldsymbol{x}, \Delta\mu); \mu_{k_n}\right) \quad \text{for} \quad n = 1, \dots, N_k, \tag{9}$$

where the transport field $\boldsymbol{c}_{k_n}(\boldsymbol{x}; \Delta\mu)$ is evaluated at the unsampled parameter variation, $\Delta\mu = \mu^* - \mu_{k_n}$, and the snapshots, $\boldsymbol{u}(\boldsymbol{x}, \mu_{k_n})$ for $n = 1, \dots, N_k$, are a subset of the solution snapshots computed off-line, $\mu_{k_n} \in \mu_s$.

Finally, the generalized coordinates, $\boldsymbol{a}(\mu^*)$, are identified by minimizing the residual of the Petrov-Galerkin expansion, ie,

$$(\boldsymbol{v}_n, \boldsymbol{R}(\boldsymbol{u}_r; \mu^*))_\Omega, \tag{10}$$

where $(\cdot, \cdot)_\Omega$ is the standard inner product as defined in Equation (5).

In summary, a new solution at an unsampled parameter using our proposed approach is given by a linear superposition of transported snapshots. This approach can be decomposed into the standard off-line–online strategy, where the transport fields are identified off-line, whereas the residual of the Petrov-Galerkin projection is minimized at the online stage.

Remark 1. The transport fields in Equation (9) are identified off-line via a training procedure. Clearly, any direct identification procedure for these fields would be intractable for large-scale systems and, very likely, yield an overdetermined and ill-conditioned system. These computational issues can be avoided by adding smoothness constraints to the transport fields. Details of this procedure are outlined in Section 3.1.

Remark 2. For the sake of brevity, we have summarized the approach for 1D parameter variations. However, the extension of this method to multidimensional parameter variations is straightforward, and the details of this extension are provided in Section 4.

Remark 3. In practice, FOMs are typically derived in a semidiscrete form by discretizing a system of PDEs in space. Hence, usually, the solution snapshots are available only as vectors and not as functions. Consequently, it is not possible to simply *evaluate* the transported snapshots for arbitrary transport field $\boldsymbol{c}_{k_n}(\boldsymbol{x}, \Delta\mu)$, as shown in Equation (9). For discrete models, this step must be performed using a numerical interpolation procedure. Computational details of this procedure are outlined in Section 5.

Remark 4. Since the reduced bases are parameter dependent, for every new prediction at an unsampled parameter, an entire set of new reduced bases must be generated. However, the computational costs of generating these bases can be expected to be proportional to the size of the FOM. Furthermore, the computational cost associated with the computation of the nonlinear residual function also scales with the size of the FOM. This expensive cost of residual evaluation can be mitigated by the precomputation of certain terms that contain polynomial nonlinearities. However, such a precomputation procedure may not be viable for other classes of nonlinear functions. Hence, to gain significant amounts of computational speedup, a hyper-reduction strategy must be utilized. Details of this procedure are outlined in Section 6.

3.1 | Off-line stage

Given the set of snapshots at sampled parameters μ_s, the methodology for identifying the transport fields $\boldsymbol{c}_s(\boldsymbol{x}; \Delta\mu)$, for $s = 1, \dots, N_s$, where $\Delta\mu = \mu - \mu_s$, for each snapshot is explained in this section.

As mentioned in Remark 1 of Section 3, to make the identification procedure for the transport field tractable for large systems, smoothness constraints are required. More precisely, since the transport fields are assumed to be smooth in space, they can be approximated using a low-order polynomial expansion in space using spatial basis functions $\boldsymbol{f}_p(\boldsymbol{x})$. The basis functions $\boldsymbol{f}_p(\boldsymbol{x})$ are selected *a priori*, such as Chebyshev polynomials or Fourier modes. Then, similar to polynomial fitting, the transport field is expressed as a polynomial expansion in parameter space as

$$\boldsymbol{c}_s(\boldsymbol{x}; \Delta\mu) = \sum_{p=1}^{N_p} \sum_{q=1}^{N_q} c_m^s \boldsymbol{f}_p(\boldsymbol{x}) g_q(\Delta\mu) \quad \text{for} \quad m = 1, \dots, N_p N_q, \tag{11}$$

where c_m^s are the coefficients of the expansion; N_p and N_q are the number of functions $\boldsymbol{f}_p(\boldsymbol{x})$ and $g_q(\Delta\mu)$, respectively; and $g_q(\Delta\mu)$ are the monomials given by

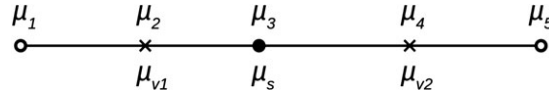$$g_q(\Delta\mu) = (\Delta\mu)^q \quad \text{for} \quad q = 1, \dots, N_q, \tag{12}$$

FIGURE 2 Schematic for choosing training snapshots

where $\Delta\mu = \mu - \mu_s$. The choice of the basis functions $\boldsymbol{f}_p(\boldsymbol{x})$ is problem dependent; hence, it is detailed in Section 8 with the help of test problems.

The least squares fitting procedure to identify the coefficients $\boldsymbol{c}^s := c_m^s$ is now explained. First, a subset of N_v solution snapshots $\boldsymbol{u}(\boldsymbol{x}; \mu_{v_n})$ for $n = 1, \ldots, N_v$, where $\mu_{v_n} \in \mu_s$, is chosen. Here, the parameters μ_{v_n} are called the training parameters for the parameter μ_s, and the corresponding snapshots are called training snapshots. The procedure for selecting N_v training snapshots from N_s is described in Section 3.1.1. The coefficients $\boldsymbol{c}^s$ are evaluated by minimizing the least squares training error between the transported snapshot $\boldsymbol{u}(\boldsymbol{x} + \boldsymbol{c}_s(\boldsymbol{x}; \Delta\mu); \mu_s)$ and training snapshots $\boldsymbol{u}(\boldsymbol{x}; \mu_{v_n})$, ie,

$$\min_{\boldsymbol{c}^s} \sum_{n=1}^{N_v} (\epsilon_n, \epsilon_n)_\Omega, \tag{13}$$

where $\epsilon_n(\boldsymbol{x}) = \boldsymbol{u}(\boldsymbol{x} + \boldsymbol{c}_s(\boldsymbol{x}; \Delta\mu); \mu_s) - \boldsymbol{u}(\boldsymbol{x}; \mu_{v_n})$; $\Delta\mu = \mu_{v_n} - \mu_s$ and $(\cdot, \cdot)_\Omega$ is the standard inner product as defined in Equation (5). The optimization problem (13) is solved N_s times for the coefficients $\boldsymbol{c}^s$ for $s = 1, \ldots, N_s$ snapshots.

In summary, the identification of the transport field in Equation (11) is posed as a least squares fitting problem for the coefficients of the polynomial fitting function.

3.1.1 | Choice of training snapshots

According to Equation (7), a snapshot at μ_{j+k} can be approximated by transporting its neighboring snapshot at μ_j. The accuracy of this approximation tends to decrease as the absolute value, $|k|$, increases. Hence, N_v training snapshots are chosen, which correspond to the N_v neighboring snapshots to $\boldsymbol{u}(\boldsymbol{x}; \mu_s)$ in the parameter space.

For instance, consider the sampled parameters $\mu_1 < \cdots < \mu_5$ in Figure 2. For the evaluation of the transport field for the snapshot at μ_3, we have $\mu_s = \mu_3$. The snapshot at μ_3 has $N_v = 2$ nearest neighboring snapshots at μ_2 and μ_4, which form the training snapshots μ_{v_1} and μ_{v_2}, respectively. It is noted that the off-line training procedure does not restrict itself to $N_v = 2$ and allows for more neighboring snapshots to be incorporated. Finally, a biased stencil can be used at the boundary of the parameter space for the selection of the training snapshots.

3.2 | Online stage

At this stage, parameter-dependent reduced bases $\boldsymbol{u}_n(\boldsymbol{x}; \mu^*)$ at an unsampled parameter $\mu^* (\neq \mu_s)$ are constructed, and generalized coordinates $\boldsymbol{a}(\mu^*)$ are identified.

For a parameter μ^* in the predictive regime, local reduced bases $\boldsymbol{u}_n$ are evaluated by transporting local snapshots $\boldsymbol{u}(\boldsymbol{x}; \mu_{k_n})$ for $n = 1, \ldots, N_k$, as shown in Equation (9), where $\mu_{k_n} \in \mu_s$ is a subset of snapshot solutions. The procedure for selecting the subset of snapshots $\boldsymbol{u}(\boldsymbol{x}; \mu_{k_n})$ is described in Section 3.2.1. For the predictive regime, the transport field $\boldsymbol{c}_{k_n}(\boldsymbol{x}; \Delta\mu)$ in Equation (11), identified at the off-line stage, is evaluated at the unsampled parameter, $\Delta\mu = \mu^* - \mu_{k_n}$.

Finally, the generalized coordinates are obtained by solving the minimization problem (16). The initial guesses for generalized coordinates at the unsampled parameter $\boldsymbol{a}(\mu^*)^{(0)}$ are obtained by a linear combination of the generalized coordinates at the known snapshots, $\boldsymbol{a}(\mu_{k_n})$. The generalized coordinates at the known snapshots are given by $\boldsymbol{a}(\mu_{k_n}) = \boldsymbol{e}_{k_n}$, where $\boldsymbol{e}_{k_n} \in \mathbb{R}^{N_k}$ is the k_nth canonical unit vector. The weights of the linear combination are obtained such that they are inversely proportional to $|\Delta\mu|$ and the sum of all weights is equal to 1.

3.2.1 | Choice of basis

In traditional projection-based MOR applied to smooth elliptic problems, ROM performance is expected to improve by increasing the number of bases N_k. Unfortunately, this is usually not the case when the solutions of interest are characterized by strong shocks and discontinuities. For example, Abgrall et al[50] demonstrated that optimal constructions of such solutions are typically sparse in the generalized coordinates and local in the parameter space. This property was also demonstrated in the nozzle problem considered in Section 2.3. Therefore, in this work, we use only a small number of local bases corresponding to N_k nearest neighboring snapshots selected from the set of N_s snapshots.
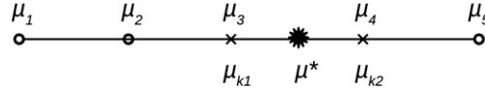
FIGURE 3 Schematic for choosing the snapshots for basis construction

For instance, consider the same sampled parameters $\mu_1 < \dots < \mu_5$ in Figure 3. For the prediction at a new unsampled parameter μ^*, $N_k = 2$ nearest neighboring snapshots are given by μ_3 and μ_4, which form the snapshots μ_{k_1} and μ_{k_2}, respectively, required for constructing the transported snapshots or local bases. It is noted that the proposed transported snapshot model order reduction (TSMOR) approach does not restrict itself to $N_k = 2$ bases and allows for more snapshots to be incorporated. Finally, for μ^* lying outside of the sampled parameter space (ie, $\mu^* < \mu_1$ or $\mu^* > \mu_5$), a biased stencil can be used for the selection of the neighboring snapshots.

4 | EXTENSION OF TSMOR TO MULTIDIMENSIONAL PARAMETER VARIATIONS

In this section, the proposed TSMOR approach is detailed for multidimensional parameter variations where the snapshots are sampled on a Cartesian grid in parameter space, $\boldsymbol{\mu} \in \mathcal{D} \subset \mathbb{R}^{N_d}$. Without loss of generality, the parameter vector $\boldsymbol{\mu} \in \mathbb{R}^{N_d}$ is normalized to fit in a hypercube such that every element of the parameter vector satisfies $-1 \leq \mu_i \leq 1$.

TSMOR for the multidimensional case proceeds exactly in the same manner as that for the 1D case but with the difference that the 1D parameter μ and parameter variation $\Delta\mu$ are replaced by the corresponding vectors $\boldsymbol{\mu}$ and $\boldsymbol{\Delta\mu}$, respectively. Consequently, solutions at an unsampled parameter $\boldsymbol{\mu}^* \neq \boldsymbol{\mu}_s$ are approximated as a linear superposition of parameter-dependent basis functions, ie,

$$\boldsymbol{u}(\boldsymbol{x}; \boldsymbol{\mu}^*) \approx \boldsymbol{u}_r = \sum_{n=1}^{N_k} \boldsymbol{u}_n(\boldsymbol{x}; \boldsymbol{\mu}^*) a_n(\boldsymbol{\mu}^*), \tag{14}$$

where the reduced-basis functions, $\boldsymbol{u}_n$, correspond to the *transported* local snapshots

$$\boldsymbol{u}_n = \boldsymbol{u}\left(\boldsymbol{x} + \boldsymbol{c}_{k_n}(\boldsymbol{x}, \boldsymbol{\Delta\mu}); \boldsymbol{\mu}_{k_n}\right) \quad \text{for} \quad n = 1, \dots, N_k, \tag{15}$$

where the transport field $\boldsymbol{c}_{k_n}(\boldsymbol{x}; \boldsymbol{\Delta\mu})$ is evaluated at the unsampled parameter variation, $\boldsymbol{\Delta\mu} = \boldsymbol{\mu}^* - \boldsymbol{\mu}_{k_n}$, and the snapshots, $\boldsymbol{u}(\boldsymbol{x}, \boldsymbol{\mu}_{k_n})$ for $n = 1, \dots, N_k$, are a subset of the solution snapshots computed off-line, $\boldsymbol{\mu}_{k_n} \in \boldsymbol{\mu}_s$.

Finally, the generalized coordinates $\boldsymbol{a}(\boldsymbol{\mu}^*)$ are identified by minimizing the residual of the Petrov-Galerkin expansion. Thus, we have

$$(\boldsymbol{v}_n, \boldsymbol{R}(\boldsymbol{u}_r; \boldsymbol{\mu}^*))_\Omega, \tag{16}$$

where $(\cdot, \cdot)_\Omega$ is the standard inner product as defined in Equation (5).

The proposed TSMOR approach for the multidimensional case is also decomposed into the standard off-line–online strategy, where the transport fields are identified off-line, whereas the residual of the Petrov-Galerkin projection is minimized at the online stage.

4.1 | Off-line stage

Given the set of snapshots at sampled parameters $\boldsymbol{\mu}_s$, the methodology for identifying the transport fields $\boldsymbol{c}_s(\boldsymbol{x}; \boldsymbol{\Delta\mu})$, for $s = 1, \dots, N_s$, where $\boldsymbol{\Delta\mu} = \boldsymbol{\mu} - \boldsymbol{\mu}_s$, for each snapshot is explained in this section.

Similar to TSMOR for 1D parameter variations, the convection field is expressed as a low-order expansion in space using spatial basis functions $\boldsymbol{f}_p(\boldsymbol{x})$. The basis functions $\boldsymbol{f}_p(\boldsymbol{x})$ are selected a priori, such as Chebyshev polynomials or Fourier modes. For the multidimensional case, the dependence of the transport field on parameter variation is modeled as a *multivariate* polynomial expansion in parameter space, ie,

$$\boldsymbol{c}_s(\boldsymbol{x}; \boldsymbol{\Delta\mu}) = \sum_{p=1}^{N_p} \sum_{q=1}^{N_q} c_m^s \boldsymbol{f}_p(\boldsymbol{x}) g_q(\boldsymbol{\Delta\mu}) \quad \text{for} \quad m = 1, \dots, N_p N_q, \tag{17}$$

where c_m^s are the coefficients of the expansion; N_p and N_q are the number of functions $\boldsymbol{f}_p(\boldsymbol{x})$ and $g_q(\Delta\boldsymbol{\mu})$, respectively; and $g_q(\Delta\boldsymbol{\mu})$ is given by

$$g_q(\Delta\boldsymbol{\mu}) = \prod_{j=1}^{N_d}(\Delta\mu_j)^{h_{q,j}} \quad \text{for } h_{q,j} \in \mathbb{Z} \quad \text{and} \quad q = 1, \dots, N_q, \tag{18}$$

where $\Delta\mu_j$ for $j = 1, \dots, N_d$ are the vectorial elements of $\Delta\boldsymbol{\mu}$. Few terms in Equation (17) are expanded using Equation (18) for clarity as

$$\boldsymbol{c}_s(\boldsymbol{x}; \Delta\boldsymbol{\mu}) = \sum_{p=1}^{N_p} c_m^s f_p(\boldsymbol{x})\Delta\mu_1 + c_{m+1}^s f_p(\boldsymbol{x})\Delta\mu_2 + \dots + c_r^s f_p(\boldsymbol{x})\Delta\mu_1^2 + c_{r+1}^s f_p(\boldsymbol{x})\Delta\mu_1\mu_2 + \dots. \tag{19}$$

Since the choice of $\boldsymbol{f}_p(\boldsymbol{x})$ is problem dependent, it is detailed in Section 8 with the help of test problems.

The least squares fitting procedure to identify the coefficients $\boldsymbol{c}^s := c_m^s$ is similar to the 1D case. First, a subset of solution snapshots $\boldsymbol{u}(\boldsymbol{x}; \boldsymbol{\mu}_{v_n})$ for $n = 1, \dots, N_v$, where $\boldsymbol{\mu}_{v_n} \in \boldsymbol{\mu}_s$, is chosen. The procedure for selecting these N_v training snapshots, $\boldsymbol{u}(\boldsymbol{x}; \boldsymbol{\mu}_{v_n})$, from N_s is described in Section 4.1.1. The coefficients $\boldsymbol{c}^s$ are evaluated by minimizing the least squares training error between the transported snapshot $\boldsymbol{u}(\boldsymbol{x} + \boldsymbol{c}_s(\boldsymbol{x}; \Delta\boldsymbol{\mu}); \boldsymbol{\mu}_s)$ and training snapshots $\boldsymbol{u}(\boldsymbol{x}; \boldsymbol{\mu}_{v_n})$, ie,

$$\min_{\boldsymbol{c}^s} \sum_{n=1}^{N_v} (\boldsymbol{\epsilon}_n, \boldsymbol{\epsilon}_n)_\Omega, \tag{20}$$

where $\boldsymbol{\epsilon}_n(\boldsymbol{x}) = \boldsymbol{u}(\boldsymbol{x} + \boldsymbol{c}_s(\boldsymbol{x}; \Delta\boldsymbol{\mu}); \boldsymbol{\mu}_s) - \boldsymbol{u}(\boldsymbol{x}; \boldsymbol{\mu}_{v_n})$; $\Delta\boldsymbol{\mu} = \boldsymbol{\mu}_{v_n} - \boldsymbol{\mu}_s$ and $(\cdot, \cdot)_\Omega$ is the standard inner product as defined in Equation (5). The optimization problem (20) is solved N_s times for the coefficients $\boldsymbol{c}^s$ for $s = 1, \dots, N_s$ snapshots.

In summary, the transport field in Equation (17) is identified by solving a least squares fitting problem for the coefficients of the polynomial fitting function.

4.1.1 | Choice of training snapshots

Similar to 1D parameter variations, N_v training snapshots are chosen, which correspond to the N_v nearest neighboring snapshots to $\boldsymbol{u}(\boldsymbol{x}; \boldsymbol{\mu}_s)$.

For instance, consider the sampled parameters in a two-dimensional (2D) parameter space denoted as "×," "∘," and "•," as shown in Figure 4. For the evaluation of the transport field for the snapshot at $\boldsymbol{\mu}_s$, $N_v = 8$ nearest neighboring snapshots denoted as "×" are chosen, which form the training snapshots $\boldsymbol{\mu}_{v_1}$ through $\boldsymbol{\mu}_{v_8}$. The three-dimensional (3D) analog would use $N_v = 26$ neighboring snapshots for the off-line training procedure and extends similarly for higher dimensions. Finally, a biased stencil can be used at the boundary of the parameter space for the selection of the training snapshots.

4.2 | Online stage

At this stage, parameter-dependent reduced bases $\boldsymbol{u}_n(\boldsymbol{x}; \boldsymbol{\mu}^*)$ at an unsampled parameter $\boldsymbol{\mu}^* \neq \boldsymbol{\mu}_s$ are constructed, and generalized coordinates $\boldsymbol{a}(\boldsymbol{\mu}^*)$ are identified.

For a parameter $\boldsymbol{\mu}^*$ in the predictive regime, local reduced bases $\boldsymbol{u}_n$ are evaluated by transporting local snapshots $\boldsymbol{u}(\boldsymbol{x}; \boldsymbol{\mu}_{k_n})$ for $n = 1, \dots, N_k$, as shown in Equation (15), where $\boldsymbol{\mu}_{k_n} \in \boldsymbol{\mu}_s$ is a subset of snapshot solutions. The procedure
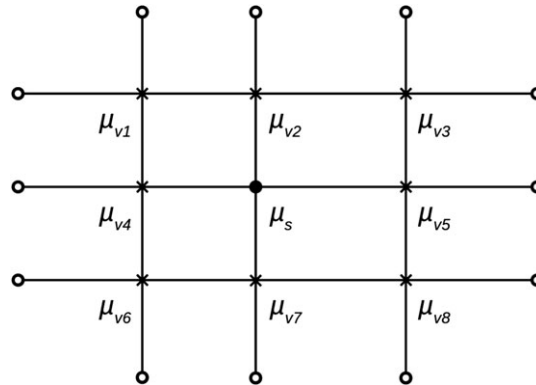

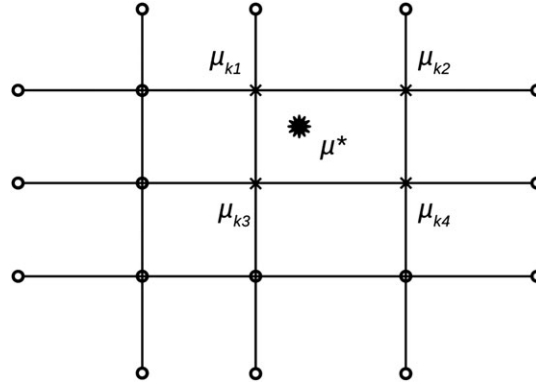**FIGURE 4** Schematic for choosing training snapshots for the two-dimensional parametrical case

FIGURE 5 Schematic for choosing the snapshots for basis construction for the two-dimensional parametrical case

for selecting the snapshots $\boldsymbol{u}(\boldsymbol{x}; \mu_{k_n})$ is described in Section 4.2.1. For the predictive regime, the transport field $\boldsymbol{c}_{k_n}(\boldsymbol{x}; \Delta\boldsymbol{\mu})$ in Equation (17), identified at the off-line stage, is evaluated at the unsampled parameter, $\Delta\boldsymbol{\mu} = \boldsymbol{\mu}^* - \boldsymbol{\mu}_{k_n}$.

Finally, the generalized coordinates are obtained by solving the minimization problem (16). The initial guesses for the generalized coordinates at the unsampled parameter $\boldsymbol{a}(\boldsymbol{\mu}^*)^{(0)}$ are obtained by a linear combination of the generalized coordinates at the known snapshots, $\boldsymbol{a}(\boldsymbol{\mu}_{k_n})$. The generalized coordinates at the known snapshots are given by $\boldsymbol{a}(\boldsymbol{\mu}_{k_n}) = \boldsymbol{e}_{k_n}$, where $\boldsymbol{e}_{k_n} \in \mathbb{R}^{N_k}$ is the k_nth canonical unit vector. The weights of the linear combination are obtained such that they are inversely proportional to $\|\Delta\boldsymbol{\mu}\|_2$ and the sum of all weights is equal to 1.

4.2.1 | Choice of basis

Similar to the 1D case, we use only a small number of local bases corresponding to the N_k nearest neighboring snapshots selected from the set of N_s snapshots.

For instance, consider the same sampled parameters in a 2D parameter space denoted as "×" and "○," as shown in Figure 5. For the prediction at a new unsampled parameter $\boldsymbol{\mu}^*$, $N_k = 4$ nearest neighboring snapshots denoted as "×" are chosen, which form the snapshots $\boldsymbol{\mu}_{k_1}$ through $\boldsymbol{\mu}_{k_4}$ required for constructing the transported snapshots or local bases. It is noted that the proposed TSMOR approach does not restrict itself to $N_k = 4$ bases and allows for more snapshots to be incorporated for this 2D case. The 3D analog would use $N_v = 8$ neighboring snapshots for basis construction and extends similarly for higher dimensions. Finally, for $\boldsymbol{\mu}^*$ lying outside of the sampled parameter space, a biased stencil can be used for the selection of the neighboring snapshots.

5 | IMPLEMENTATION OF TSMOR IN THE DISCRETE FRAMEWORK

As mentioned in Remark 3 of Section 3, FOM solutions are typically available as vectors of state variables specified at various spatial locations. Thus, this section discusses the implementation strategy for applying the proposed TSMOR approach in the discrete framework.

Let $\boldsymbol{w}(\boldsymbol{\mu}_s) \in \mathbb{R}^{N_w}$ denote the discrete FOM solution of the snapshot solution $\boldsymbol{u}(\boldsymbol{x}; \boldsymbol{\mu}_s)$. In the continuous form, the transported snapshot $\boldsymbol{u}(\boldsymbol{x} + \boldsymbol{c}_s(\boldsymbol{x}; \Delta\boldsymbol{\mu}); \boldsymbol{\mu}_s)$, where $\Delta\boldsymbol{\mu} = \boldsymbol{\mu} - \boldsymbol{\mu}_s$, is directly evaluated by computing the solution at the new spatial locations $\boldsymbol{x} + \boldsymbol{c}_s(\boldsymbol{x}; \Delta\boldsymbol{\mu})$. However, in the discrete form, an interpolation step is required to evaluate the transported snapshots. More specifically, if $\boldsymbol{w}(\boldsymbol{\mu}_s)$ is the vector of state variables on a computational grid with Cartesian coordinates $\boldsymbol{x}_i \in \mathbb{R}^{N_w}$ for $i = 1, 2, 3$, then the transported solution snapshot is evaluated by interpolating $\boldsymbol{w}(\boldsymbol{\mu}_s)$ from $\boldsymbol{x}_i + \boldsymbol{c}_s(\boldsymbol{x}_i; \Delta\boldsymbol{\mu})$ to the original grid $\boldsymbol{x}_i$. In the discrete form, $\boldsymbol{c}_s(\boldsymbol{x}_i; \Delta\boldsymbol{\mu}) \in \mathbb{R}^{N_w}$ denotes the transport field in Equation (17) evaluated at $\boldsymbol{x}_i$ grid points, and the transported snapshot from $\boldsymbol{\mu}_s$ to $\boldsymbol{\mu}$ is denoted as $\boldsymbol{w}'(\boldsymbol{\mu}_s, \boldsymbol{\mu}) \in \mathbb{R}^{N_w}$.

Consequently, the solution at the new parameter using the TSMOR approach is given by

$$\boldsymbol{w}(\boldsymbol{\mu}^*) \approx \boldsymbol{w}_r(\boldsymbol{\mu}^*) = \boldsymbol{U}(\boldsymbol{\mu}^*)\boldsymbol{a}(\boldsymbol{\mu}^*), \tag{21}$$

where $\boldsymbol{U}(\boldsymbol{\mu}^*) \in \mathbb{R}^{N_w \times N_k}$ is a matrix whose columns contain the *transported* solution snapshots $\boldsymbol{w}'(\boldsymbol{\mu}_{k_n}, \boldsymbol{\mu}^*)$ of the corresponding snapshots $\boldsymbol{w}(\boldsymbol{\mu}_{k_n})$. More precisely, $\boldsymbol{U}(\boldsymbol{\mu}^*)_{:,n} := \boldsymbol{w}'(\boldsymbol{\mu}_{k_n}, \boldsymbol{\mu}^*)$, where the subscript $(:, n)$ denotes the nth column of a matrix. The generalized coordinates $\boldsymbol{a}(\boldsymbol{\mu}^*)$ are chosen to minimize the residual at the new parameter $\boldsymbol{\mu}^*$, ie,

$$\min_{\boldsymbol{a}} \|\boldsymbol{R}(\boldsymbol{U}(\boldsymbol{\mu}^*)\boldsymbol{a}(\boldsymbol{\mu}^*); \boldsymbol{\mu}^*)\|_p, \tag{22}$$

where $\|\cdot\|_p$ is the standard ℓ_p-norm. For $p = 2$, this residual minimization (22) is equivalent to an LSPG projection of the residual equation in the continuous framework given by (16) with test basis $\mathbf{v}_n = \mathbf{J}\mathbf{u}_n$, where $\mathbf{J} = \partial \mathbf{R}/\partial \mathbf{a}$ denotes the Jacobian of the residual.

Similarly, the least squares minimization problem (20) in discrete form can be expressed as

$$\min_{\mathbf{c}^s} \sum_{n=1}^{N_v} \left\| \mathbf{w}'(\boldsymbol{\mu}_s, \boldsymbol{\mu}_{v_n}) - \mathbf{w}(\boldsymbol{\mu}_{v_n}) \right\|_2^2. \tag{23}$$

Remark 5. The evaluation of the transported snapshot in the discrete form faces a drawback of the possibility of negative volume elements. Since it is usually not possible to evaluate the solution residual and perform interpolation on a computational grid with negative volume elements, the training error minimization problem (20) can be augmented with inequality constraints for the volume elements, ie,

$$\min_{\mathbf{c}^s} \sum_{n=1}^{N_v} \left\| \mathbf{w}'(\boldsymbol{\mu}_s, \boldsymbol{\mu}_{v_n}) - \mathbf{w}(\boldsymbol{\mu}_{v_n}) \right\|_2^2 \tag{24}$$

$$\text{subject to} \quad V_j > \delta_v, \quad \text{for} \quad j = 1, \dots, N_V,$$

where V_j are the N_V element volumes and $\delta_v > 0$ is the minimal positive volume. For a structured Cartesian grid, this constraint simplifies to $(x_i')_{j+1} - (x_i')_j > \delta_v$ for $i = 1, 2, 3$ and $j = 1, \dots, N_V$, where $x_i' = x_i + c_s(x_i; \Delta\boldsymbol{\mu})$.

Remark 6. Since the transported snapshot $\mathbf{w}'(\boldsymbol{\mu}_s, \boldsymbol{\mu}_{v_n})$ is an approximation of the snapshot $\mathbf{w}(\boldsymbol{\mu}_{v_n})$, $\mathbf{w}'(\boldsymbol{\mu}_s, \boldsymbol{\mu}_{v_n})$ should satisfy the boundary conditions corresponding to the parameter $\boldsymbol{\mu}_{v_n}$. Generally, for a large class of problems, linear extrapolation at the boundaries of the computational domain (during the interpolation of $\mathbf{w}(\boldsymbol{\mu}_s)$ from $x_i + c_s(x_i; \Delta\boldsymbol{\mu})$ to x_i) is found to be a reasonable approximation of the boundary conditions for low to moderate parameter variations. However, an approximation of boundary conditions by extrapolation would be a poor choice if the desired boundary conditions have sharp gradients or discontinuities. To tackle this issue, the transport of the boundary nodes can be restricted such that the need for extrapolation is avoided. The transport of the boundary nodes can be restricted by enforcing appropriate conditions on the coefficients $\mathbf{c}^s$ of the transport $c_s(x_i; \Delta\boldsymbol{\mu})$. Since this issue is problem dependent, it is discussed in detail in Section 8 with the help of test problems.

Remark 7 (Choice of norms, l_p).

In traditional projection-based MOR, the generalized coordinates are usually selected to minimize the ℓ_2-norm of the residual. Although this approach has been demonstrated to work adequately for many applications, in the case when the FOM is comprised of a system of hyperbolic conservation laws, minimizing the ℓ_1-norm has been shown to be preferable.[50] For our proposed approach, the ℓ_1-norm for the residual minimization (22) is found to perform better than other choices of norms. Unfortunately, the optimal choice of norm remains an open problem.

The classical approach for solving the ℓ_1-norm minimization problems involves recasting the problem as a linear program or, alternatively, solving iteratively using, for example, iteratively reweighted least squares.[51,52] The methodology for minimizing the ℓ_1-norm is also explained in the work of Abgrall et al.[50]

5.1 | Summary of TSMOR

The off-line and online stages of the proposed TSMOR approach in the discrete framework are summarized in Algorithms 1 and 2, respectively.

Algorithm 1 TSMOR−off-line stage
Input: Steady-state snapshots, $\mathbf{w}(\boldsymbol{\mu}_s)$ for $s = 1, \dots, N_s$
Output: Coefficients, $\mathbf{c}^s$ for $s = 1, \dots, N_s$
1: **for** $s \leftarrow 1$ to N_s **do**
2: Determine N_v training snapshots $\mathbf{w}(\boldsymbol{\mu}_{v_n})$ for $n = 1, \dots, N_v$ as mentioned in Section 4.1.1
3: Determine $\Delta\boldsymbol{\mu} = \boldsymbol{\mu}_{v_n} - \boldsymbol{\mu}_s$ for $n = 1, \dots, N_v$
4: Select basis functions, $f_p(x)$ and determine $g_q(\Delta\boldsymbol{\mu})$ from Equation (18)
5: Define transport fields $c_s(x; \Delta\boldsymbol{\mu})$ using Equation (17)
6: Compute transported snapshots $\mathbf{w}'(\boldsymbol{\mu}_s, \boldsymbol{\mu}_{v_n})$ by interpolating $\mathbf{w}(\boldsymbol{\mu}_s)$ from $x_i + c_s(x_i; \Delta\boldsymbol{\mu})$ to the original grid x_i
7: Solve training error minimization problem (23) or (24) for the coefficients $\mathbf{c}^s$
8: **end for**

Algorithm 2 TSMOR−online stage

Input: $w(\mu_s)$ and c^s for $s = 1, \ldots, N_s$; Basis functions, $f_p(x)$; Unsampled parameter, μ^*

Output: Solution prediction, $w_r(\mu^*)$

1: Determine N_k local snapshots $w(\mu_{k_n})$ for $n = 1, \ldots, N_k$ as mentioned in Section 4.2.1
2: Determine $\Delta\mu = \mu^* - \mu_{k_n}$ for $n = 1, \ldots, N_k$
3: Determine $g_q(\Delta\mu)$ from Equation (18)
4: Compute transports $c_{k_n}(x_i; \Delta\mu)$ using Equation (17)
5: Compute transported snapshots $w'(\mu_{k_n}, \mu^*)$ by interpolating $w(\mu_{k_n})$ from $x_i + c_{k_n}(x_i; \Delta\mu)$ to the original grid x_i
6: Construct local basis $U(\mu^*)$ as a collection of transported snapshots, ie, $U(\mu^*)_{:,n} := w'(\mu_{k_n}, \mu^*)$
7: Solve the residual minimization problem (22) for $a(\mu^*)$
8: Compute $w_r(\mu^*)$ from Equation (21)

---

6 | HYPER-REDUCTION

At the online stage of TSMOR, an evaluation of the residual $R(U(\mu^*)a(\mu^*))$ in Equation (22) scales with the size of the FOM, N_w. Furthermore, for every new prediction at μ^*, a new parameter-dependent basis $U(\mu^*)$ has to be constructed, the computation of which also scales with N_w. Hyper-reduction can significantly reduce these computational complexities. A review of the state-of-the-art hyper-reduction techniques, such as DEIM,[47] Gauss-Newton with approximated tensors,[48] and ECSW,[49] is provided in this section. Furthermore, the methodology to equip the proposed TSMOR approach with hyper-reduction strategies is outlined.

6.1 | Review of hyper-reduction techniques

In hyper-reduction for traditional projection-based MOR described in Section 2.2, the residual $R(Ua(\mu^*))$ is evaluated only at a small subset of n_w interpolation entries $\varepsilon \subset \{1, \ldots, N_w\}$. The interpolation matrix $Z \in \mathbb{R}^{N_w \times n_w}$ is thus defined as

$$Z = \left[e_{\varepsilon_1}, e_{\varepsilon_2}, \ldots, e_{\varepsilon_{n_w}} \right], \tag{25}$$

where $e_\varepsilon \in \mathbb{R}^{N_w}$ is the εth canonical unit vector. $R(Ua(\mu^*))$ is then approximated in a low-dimensional subspace $U_R \in \mathbb{R}^{N_w \times N_R}$, ie,

$$R(Ua(\mu^*)) \approx U_R (Z^T U_R)^+ Z^T R(Ua(\mu^*)). \tag{26}$$

Finally, Equation (26) is projected on a low-dimensional subspace using state basis U. Since the computation of $Z^T R(Ua(\mu^*))$ involves the evaluation of the residual at only n_w grid locations, the resulting minimization problem is independent of the size of FOM, N_w.

Another class of hyper-reduction techniques, for instance, ECSW, involves the minimization of the weighted residuals computed only at ε points. Thus, all the computations are performed on these *collocation points*, and interpolation of the residuals using basis functions is avoided.

6.2 | Hyper-reduction applied to TSMOR

In this work, we adopt a collocation-based hyper-reduction approach similar to ECSW. More specifically, the residual minimization problem (22) in this hyper-reduction framework is written as

$$\min_a \| Z^T R(U(\mu^*)a(\mu^*); \mu^*) \|_p. \tag{27}$$

Generally, in most CFD problems, the Jacobian matrix is sparse. Hence, the computation of the residuals is dependent only on a few subset of $\hat{n}_w$ entries $\hat{\varepsilon} \subset \{1, \ldots, N_w\}$. The corresponding interpolation matrix is denoted as $P \in \mathbb{R}^{N_w \times \hat{n}_w}$. Thus, $U(\mu^*)a(\mu^*)$ can be replaced by $PP^T U(\mu^*)a(\mu^*)$, resulting in the cheap computation of the collocated reduced basis, $P^T U(\mu^*)$, whose columns contain the collocated transported snapshots, ie, $(P^T U(\mu^*))_{:,n} = P^T w'(\mu_{k_n}, \mu^*)$.

The collocated transported snapshot at the collocation points $\hat{\varepsilon}$ is computed by interpolating the collocated snapshot, $P^T w(\mu_{k_n})$, from $\hat{x}_i + \hat{c}_{k_n}(\hat{x}_i; \Delta\mu)$ to the original grid $\hat{x}_i$. Here, $\hat{c}_{k_n}(\hat{x}_i; \Delta\mu) = P^T c_{k_n}(x_i; \Delta\mu) \in \mathbb{R}^{\hat{n}_w}$ are the collocated transports, and $\hat{x}_i = P^T x_i \in \mathbb{R}^{\hat{n}_w}$ are the Cartesian coordinates of the original grid at the collocation points.

To summarize, Equation (27) involves the computation of $\mathbf{Z}^T\mathbf{R}(\mathbf{PP}^T\mathbf{U}(\boldsymbol{\mu}^*)\mathbf{a}(\boldsymbol{\mu}^*))$, which necessitates the computation of $\mathbf{R}(\mathbf{U}(\boldsymbol{\mu}^*)\mathbf{a}(\boldsymbol{\mu}^*))$ and $\mathbf{U}(\boldsymbol{\mu}^*)$ only at ε and $\hat{\varepsilon}$ indices, respectively, resulting in a reduction of the computational complexity from N_w to $\hat{n}_w$.

6.2.1 | Identification of collocation points

Various hyper-reduction techniques in the literature use different strategies for identifying the collocation points or interpolation entries ε. Generally, these approaches are specific to their respective hyper-reduction procedure. For instance, these algorithms are based on the minimization of the error in the interpolated snapshots,[47] the greedy approach to minimize the error associated with the gappy POD projection of a residual,[53] and solving a sparse nonnegative least squares problem.[49] In this work, we use the standard DEIM Algorithm 3 to identify the collocation points.

The DEIM algorithm uses basis functions $\mathbf{U}_R$ of the nonlinear residual to identify the interpolation entries ε. In our implementation of the algorithm, $\mathbf{U}_R$ are the POD bases of the snapshots of residuals. The snapshots of residuals are collected at each iteration while solving the FOM Equation (2) during the off-line stage. For boundary value problems, in addition to DEIM indices, it is important to include inlet/outlet grid points into ε since these boundary conditions contain vital information about the dynamics of the problem. Details about the inclusion of these boundary points are explained in Section 8, where this topic is covered for each flow problem. Finally, the corresponding interpolation entries $\hat{\varepsilon}$ for computing the residuals can be related to ε depending on the type of the finite difference/volume/element scheme.

Algorithm 3 DEIM

Input: POD basis of snapshots of residuals, $\mathbf{U}_R$

Output: Interpolation entries $\boldsymbol{\varepsilon} = [\varepsilon_1, \ldots, \varepsilon_{n_w}]$

1: $[\ , \varepsilon_1] = \max\{|\mathbf{U}_{R_{(:,l)}}|\}$

2: $\mathbf{V} = [\mathbf{U}_{R_{(:,l)}}], \mathbf{Z} = [\mathbf{e}_{\varepsilon_1}], \boldsymbol{\varepsilon} = [\varepsilon_1]$

3: **for** $l \leftarrow 2$ to n_w **do**

4:      Solve $(\mathbf{Z}^T\mathbf{V})c = \mathbf{P}^T\mathbf{U}_{R_{(:,l)}}$

5:      $\mathbf{r} = \mathbf{U}_{R_{(:,l)}} - \mathbf{V}c$

6:      $[\ , \varepsilon_l] = \max\{|\mathbf{r}|\}$

7:      $\mathbf{V} \leftarrow [\mathbf{V}, \mathbf{U}_{R_{(:,l)}}], \mathbf{Z} \leftarrow [\mathbf{Z}, \mathbf{e}_{\varepsilon_l}], \boldsymbol{\varepsilon} \leftarrow [\boldsymbol{\varepsilon}, \varepsilon_l]$

8: **end for**

---

7 | COMPARISON WITH PREVIOUS MOR APPROACHES

Our proposed approach shares similarities with previous parametric MOR techniques in the literature. Similar to the works of Reiss et al,[40] Iollo and Lombardi,[37] and Welper,[39] we approximate the sought-after solutions as a superposition of transported snapshots or their basis. However, the methodology to identify the transport fields and the corresponding transported snapshots is different, where our approach provides the following advantages.

The shifted-POD method,[40] developed for unsteady-flow problems, involves the identification of shift velocities on the basis of known or data-driven unsteady-transport phenomena. However, this approach has not yet been realized and demonstrated for the reduction of steady-flow problems.

The transport obtained by solving an optimal mass transfer problem[37] is optimal in the sense that the displacement of the computational domain to transform one snapshot into the other is minimal. The formulation of the optimal mass transfer problem, however, has the following issues. First, the optimal transports obtained between various pairs of snapshots may not provide an intermediate transported snapshot in the predictive regime that approximately satisfies the physics of the underlying problem. In other words, we seek a physics-based transport field instead of an optimal transport (although an optimal transport may show similarities with physics-based transport for a subset of flow problems). In our proposed approach, the transport field is evaluated by a least squares fitting procedure that minimizes the approximation error of multiple local transported snapshots. This ensures that the transport field captures the physics-based dynamics of snapshot transformation from all the neighboring snapshots. Second, it has been demonstrated for image processing applications that for images with sharp features, optimal transport can lead to numerical artifacts at these sharp edges,[54] whereas a Lagrangian approach for solving the optimal mass transfer problem can lead to diffusion of sharp boundaries.[55]

In the fluid mechanics community, these sharp features can be interpreted as shocks, implying that optimal transport may not be easily extendable for flow problems containing shocks.

In transformed snapshot interpolation (TSI),[39] the transports for approximating the solution in the predictive regime are obtained by interpolating the transports evaluated between various pairs of known snapshots. Our proposed method for identifying the transport fields can be considered as a generalization of TSI, with the difference being that our method is essentially a least squares fit in contrast to interpolation in TSI. The advantage of fitting as compared to interpolation is that the fitting polynomial can be chosen to contain fewer terms than a corresponding interpolation polynomial. This property allows for easy extension of our method to multidimensional parameter variations by mitigating the curse of dimensionality faced by TSI. Furthermore, our residual minimization approach is projection based in contrast to the interpolation-based approach in TSI. One of the potential advantages of projection-based methods is that they retain the underlying structure of the dynamical system and, thus, provide, in principle, more robust predictive capabilities.

Finally, similar to the work of Abgrall et al,[50] we minimize the system residual in the ℓ_1-norm, which has been shown to be beneficial for problems containing shocks and discontinuities.

8 | NUMERICAL EXPERIMENTS

In this section, TSMOR is applied to the steady Euler equations modeling a supersonic flow inside a quasi-1D nozzle and a 2D flow over a forward-facing step and a nonlinear advection-diffusion equation modeling a jet diffusion flame in a combustor. These problems are chosen because the steady-flow solutions contain shocks or flame fronts whose spatial locations and orientations are parameter dependent. Similar numerical experiments have been studied by Lucia et al,[44] Mojgani and Balajewicz,[42] Zahr et al,[25] Welper,[56] and Galbally et al.[57]

In this section, the results generated by the proposed TSMOR approach are compared with traditional projection-based MOR techniques, such as LSPG with test subspace $v_n = Ju_n$, as described in Section 2.2, where u_n is the POD basis of the snapshot matrix and J is the Jacobian of the residual function. Furthermore, comparison is also made with recent parametric MOR techniques, such as the L_1-dictionary approach,[50] where the solution is given by a linear combination of local snapshots or *dictionary* elements, and the L_1-norm of the residual is minimized. All results considered in this section are predictive, that is, the predicted solutions all lie in parameter regions not sampled during the off-line training phase. The performance of these MOR techniques is analyzed by computing the relative error between the predicted and FOM solutions, where the error is defined as

$$\text{Error}(\%) = \frac{||w(\mu^*) - w_r(\mu^*)||_2}{||w(\mu^*)||_2} \times 100, \tag{28}$$

where $w(\mu^*)$ and $w_r(\mu^*)$ are the FOM and predicted solutions using the abovementioned MOR methods, respectively. All the computations were done in MATLAB.

8.1 | Quasi-1D flow in a converging-diverging nozzle

8.1.1 | Problem description

The 1D Euler equations in a quasi-1D converging-diverging nozzle are considered, ie,

$$\frac{1}{A}\frac{\partial AF}{\partial x} = Q \qquad x \in [0, L], \tag{29}$$

where $A = A(x)$ is the area profile, and

$$w(\mu) = \begin{bmatrix} \rho \\ \rho u \\ \rho E \end{bmatrix}, \quad F = \begin{bmatrix} \rho u \\ \rho u^2 + p \\ (\rho E + p)u \end{bmatrix}, \quad Q = \begin{bmatrix} 0 \\ \frac{p}{A}\frac{\partial A}{\partial x} \\ 0 \end{bmatrix}$$

with homogeneous Dirichlet boundary conditions $\rho(0; \mu) = 1, p(0; \mu) = 1$, and $p(L; \mu) = 0.7$.

The boundary conditions are chosen such that a shock is formed in the diverging section of the nozzle. Length of the nozzle L is 10 units. The area profile of the converging-diverging nozzle is parabolic with equal inlet and outlet areas, $A(0) = A(L) = 3$, and the throat is located at $L/2$. For this problem, the throat area $\mu = A(L/2)$ is the parameter of interest. Steady-state solutions are obtained by discretizing the corresponding governing equations in space using a central second-order finite difference scheme on a uniform grid, which is divided into 1000 grid points with grid spacing

$\Delta x = 0.01$. A first-order accurate artificial viscosity scheme using $v = \Delta x/2$ is used to stabilize the solution. The resulting nonlinear system of algebraic equations is solved in MATLAB using the built-in `fsolve` algorithm. Figure 1A shows the steady-state density solutions for different values of throat area μ.

8.1.2 | Implementation of TSMOR

A snapshot matrix $\boldsymbol{M}$ containing four snapshots at parameters $\mu_s = [0.5, 0.875, 1.25, 1.625]$ is generated. The coefficients of the polynomial expansion (11) $\boldsymbol{c}^s$ for each snapshot are computed off-line by solving the training error minimization (24). The bases $f_p(x)$ are chosen to be Fourier sine series with m modes, ie,

$$\boldsymbol{f}(x) = \left[1, \sin\left(\frac{\pi x}{L}\right), \dots, \sin\left(\frac{(m-1)\pi x}{L}\right) \right]. \tag{30}$$

For this simple problem, $g_q(\Delta\mu)$ is given by

$$g(\Delta\mu) = \Delta\mu. \tag{31}$$

The interpolation from the transported grid to the original grid for calculating the transported snapshots was performed using the `interp1` algorithm. The training error minimization (24) is solved using the `fmincon` algorithm.

First, convergence of the proposed TSMOR approach with respect to the number of Fourier modes m is studied by predicting new solutions in the predictive regime μ^*. Figure 6A shows the mean and maximum relative errors in the TSMOR solutions predicted at two uniformly distributed parameters in every interval of μ_s for different numbers of Fourier modes m. It can be seen that as the number of Fourier modes increases, the error converges to a low value of 0.27%. The TSMOR convergence plot is compared to the convergence of LSPG solutions with respect to the number of POD bases k of the snapshot matrix $\boldsymbol{M}$. Similar to Figure 6A, Figure 6B displays the relative errors in the LSPG solutions predicted at the same set of parameters for different numbers of bases. It can be observed that the error converges only to 7.16% even though all four POD bases were used for prediction. Hereafter, all the TSMOR predicted results presented for this problem are produced with three Fourier modes.

Next, the performance of the proposed TSMOR approach is compared to several existing MOR techniques. Figure 7 illustrates the predictive capabilities of several MOR approaches for the parameters $\mu^* = 1.0$ and $\mu^* = 1.5$. The FOM density solution is given by the gray lines, whereas the new proposed TSMOR approach using two local bases corresponding to two nearby snapshots is given by the red lines. The blue lines correspond to the solution obtained by the LSPG method using four POD modes of the snapshot matrix $\boldsymbol{M}$. The green lines correspond to the L_1-dictionary approach using two local snapshots or dictionary elements. The proposed TSMOR approach reproduces the solution remarkably well. In contrast, LSPG does not predict the correct shock location, whereas L_1-dictionary solutions are dominated by staircase shock–type errors.
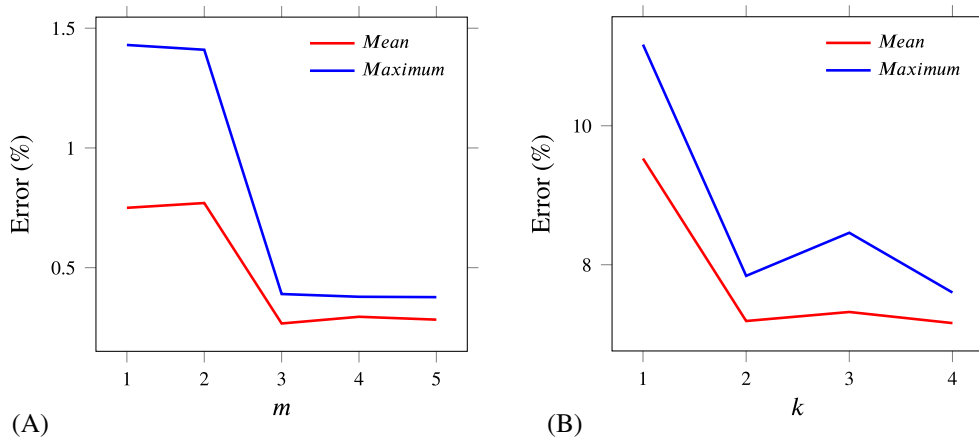

FIGURE 6 Convergence plot of the relative error for transported snapshot model order reduction (TSMOR) and least squares Petrov-Galerkin (LSPG) predicted solutions. A, Plot of relative error vs number of Fourier modes m for TSMOR predicted solutions; B, Plot of relative error vs number of proper orthogonal decomposition bases k for LSPG predicted solutions
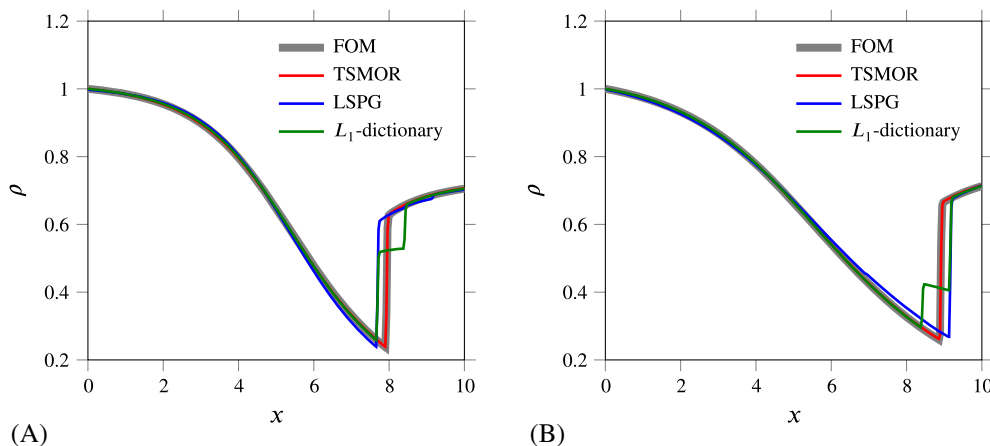
FIGURE 7 Comparison of predicted solutions using transported snapshot model order reduction (TSMOR), least squares Petrov-Galerkin (LSPG), and the L_1-dictionary approach with the full-order model (FOM). A, Predicted solutions at $\mu^* = 1.00$; B, Predicted solutions at $\mu^* = 1.50$
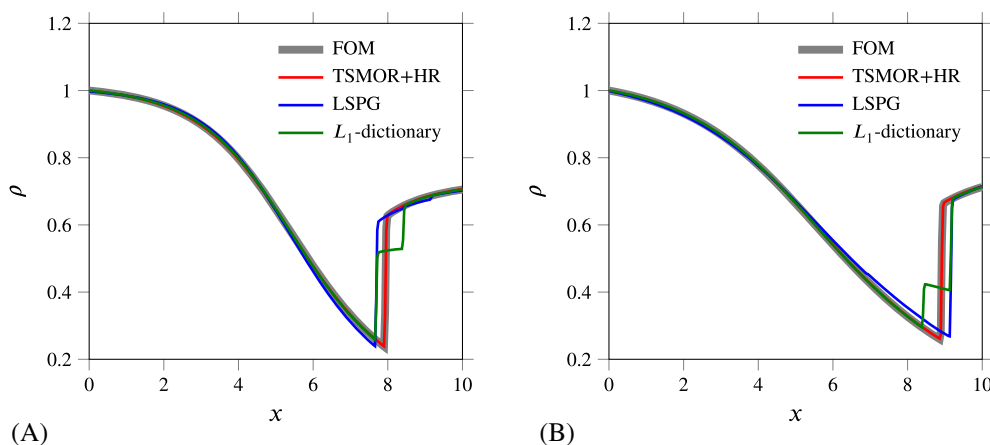

FIGURE 8 Comparison of predicted solutions using hyper-reduced transported snapshot model order reduction (TSMOR+HR), least squares Petrov-Galerkin (LSPG), and the L_1-dictionary approach with the full-order model (FOM). A, Predicted solutions at $\mu^* = 1.00$; B, Predicted solutions at $\mu^* = 1.50$

Next, the TSMOR approach is equipped with the hyper-reduction strategy mentioned in Section 6.2. First, 30 collocation points are obtained by using the DEIM algorithm. Second, these points are augmented with inlet and outlet points, $i = 1$, and $i = N_w$, respectively, if not already included in those 30 DEIM collocation points. Finally, an additional $\hat{n}_w \approx n_w \times 2 = 64$ points $\hat{\varepsilon}$ are included to enable the evaluation of the residuals via the central finite difference scheme. Figure 8 illustrates the predictive capabilities of hyper-reduced TSMOR (TSMOR+HR) for the same parameters $\mu^* = 1.0$ and $\mu^* = 1.5$. The TSMOR+HR density solutions are compared with the non–hyper-reduced LSPG and L_1-dictionary approaches. As before, excellent agreement with the FOM solution is demonstrated by TSMOR+HR.

In Figure 9, relative errors between the FOM solutions and predicted solutions using the TSMOR+HR, non–hyper-reduced LSPG, and L_1-dictionary approaches are illustrated across the entire parameter range of interest. For this case, predictions are made at two uniformly distributed parameters in every interval of μ_s. It can be observed that the solutions predicted using TSMOR+HR have an average error of only 0.27% as compared to 7.22% in LSPG and 5.88% in the L_1-dictionary approach. Thus, for all parameters considered, the TSMOR approach significantly outperforms the LSPG and L_1-dictionary methods. Finally, wall times and speedups for the FOM and the online stage of TSMOR+HR are illustrated in Figure 10A and 10B, respectively. Here, speedup is defined as the ratio of wall times of the FOM to the online stage of TSMOR+HR. TSMOR+HR delivers a speedup of approximately four orders of magnitude across the entire parameter range while maintaining a high level of accuracy.
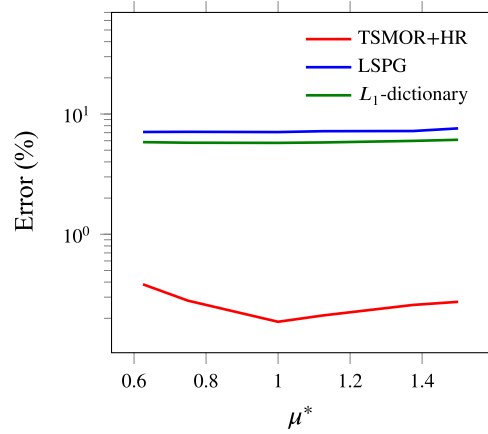
FIGURE 9 Performance comparison between hyper-reduced transported snapshot model order reduction (TSMOR+HR), least squares Petrov-Galerkin (LSPG), and the L_1-dictionary approach for solution predictions at various parameters
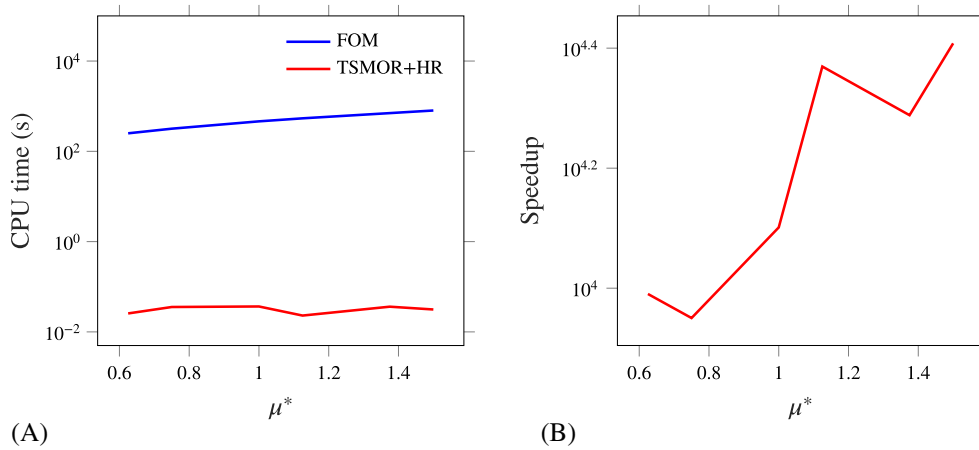

FIGURE 10 Comparison of the central processing unit (CPU) wall time associated with the full-order model (FOM) and the online stage of hyper-reduced transported snapshot model order reduction (TSMOR+HR) for solution predictions at various parameters. A, CPU wall time; B, Speedup achieved by TSMOR+HR

8.2 | Supersonic flow over a forward-facing step

8.2.1 | Problem description

This problem consists of a supersonic flow over a 2D forward-facing step in a wind tunnel setup with walls on top and bottom, as described in the work of Woodward and Colella[58] and also shown in Figure 11A. The length (L) and height (H) of the wind tunnel are 3 units and 1 unit, respectively. The step has a height of 0.2 units and is located at the bottom wall starting at 0.6 units from the left end of the tunnel. Two-dimensional Euler equations governing the supersonic flow over a forward-facing step are

$$\frac{\partial \boldsymbol{F}}{\partial x} + \frac{\partial \boldsymbol{G}}{\partial y} = 0, \qquad x \in [0, L], \quad y \in [0, H], \tag{32}$$

where

$$\boldsymbol{w}(\mu) = \begin{bmatrix} \rho \\ \rho u \\ \rho v \\ \rho E \end{bmatrix}; \boldsymbol{F} = \begin{bmatrix} \rho u \\ \rho u^2 + p \\ \rho uv \\ (\rho E + p)u \end{bmatrix}; \boldsymbol{G} = \begin{bmatrix} \rho v \\ \rho uv \\ \rho v^2 + p \\ (\rho E + p)v \end{bmatrix}$$

with homogeneous Dirichlet inlet boundary conditions $\rho(0, y; \mu) = 1.4, p(0, y; \mu) = 1, u(0, y; \mu) = \mu$, and $v(0, y; \mu) = 0$, where μ is the inlet supersonic Mach number that is taken to be the varying parameter of interest. No penetration solid wall
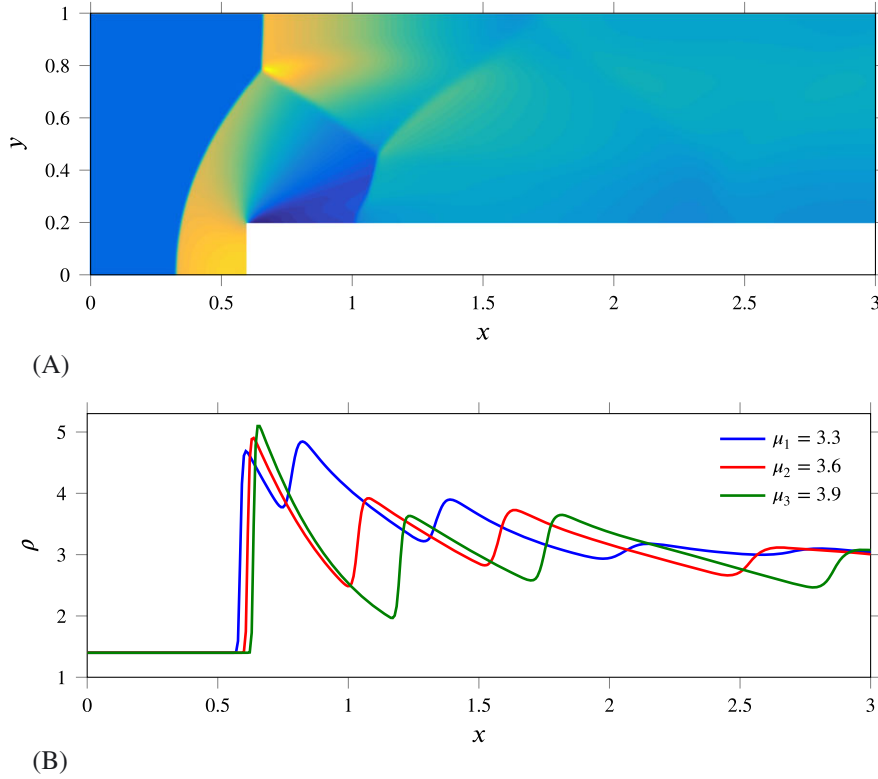
FIGURE 11 Steady-state density plots of a supersonic flow over a forward-facing step. A, Steady-state density contour for the inlet Mach number $\mu = 3.3$; B, One-dimensional steady-state density plots at $y = 0.7$ for the inlet Mach number μ

boundary conditions are imposed on the top, bottom, and step wall surfaces. The equations are discretized in space using a second-order, central finite difference scheme on a uniform Cartesian grid that is divided into 0.48 million grid points with $\Delta x = \Delta y = 0.025$. The solutions are stabilized using a first-order artificial viscosity scheme where the artificial viscosity is set to be $\nu = \Delta x / 0.8$. The resulting equations are solved by marching to steady state using a second-order strong stability preserving Runge-Kutta scheme.[59] Figure 11A shows the steady-state density contour for the inlet Mach number $\mu = 3.3$, whereas the corresponding 1D plots at $y = 0.7$ for the inlet Mach numbers $\mu = 3.3$, 3.6, and 3.9 are shown in Figure 11B.

8.2.2 | Implementation of TSMOR

A snapshot matrix $\boldsymbol{M}$ containing five snapshots at parameters $\mu_s = [3.3, 3.45, 3.6, 3.75, 3.9]$ is generated. The coefficients of the polynomial expansion (17) $\boldsymbol{c}^s$ for each snapshot are computed off-line by solving the training error minimization (24). The bases of the polynomial expansion, $f_{x_p}(x)$ and $f_{y_p}(y)$, for the x and y transport fields, $c_{s_x}(x, \Delta\mu)$ and $c_{s_y}(y, \Delta\mu)$, respectively, are chosen to be Fourier sine series with m modes each, ie,

$$\boldsymbol{f}_x(x) = \left[1, \sin\left(\frac{\pi x}{L}\right), \ldots, \sin\left(\frac{(m-1)\pi x}{L}\right)\right]$$

$$\boldsymbol{f}_y(y) = \left[1, \sin\left(\frac{\pi y}{H}\right), \ldots, \sin\left(\frac{(m-1)\pi y}{H}\right)\right], \tag{33}$$

and $g_q(\Delta\mu)$ is given by

$$\boldsymbol{g}(\Delta\mu) = \left[\Delta\mu, \Delta\mu^2\right]. \tag{34}$$

The interpolation from the transported grid $(x + c_{s_x}(x; \Delta\mu), y + c_{s_y}(y; \Delta\mu))$ to the original grid (x, y) for calculating the transported snapshots was performed using the `interp2` algorithm in MATLAB. The training error minimization (24) is solved using the `fmincon` algorithm.

First, the convergence of the proposed TSMOR approach with respect to the number of Fourier modes m is studied by predicting new solutions in the predictive regime μ^*. Figure 12A shows the mean and maximum relative errors in
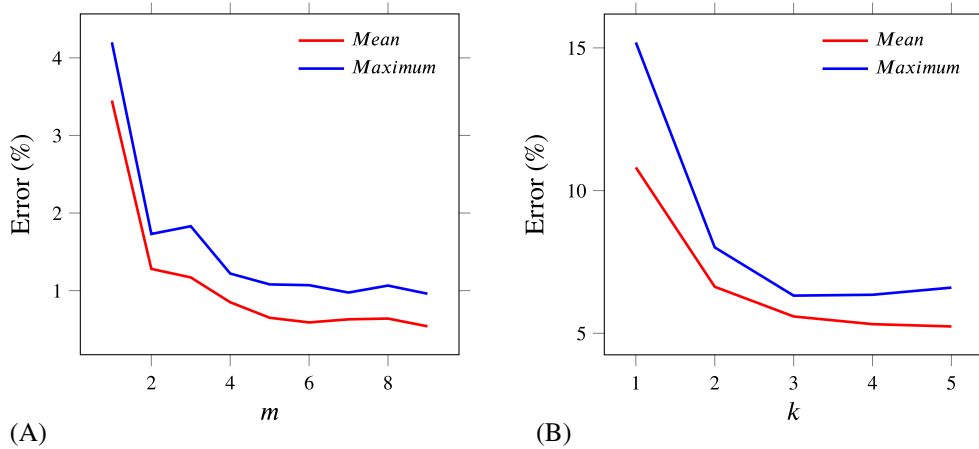
FIGURE 12 Convergence plot of the relative error for transported snapshot model order reduction (TSMOR) and least squares Petrov-Galerkin (LSPG) predicted solutions. A, Plot of relative error vs number of Fourier modes m for TSMOR predicted solutions; B, Plot of relative error vs number of proper orthogonal decomposition bases k for LSPG predicted solutions

the TSMOR solutions predicted at two uniformly distributed parameters in every interval of μ_s for different numbers of Fourier modes m. It can be seen that as the number of Fourier modes increases, the error converges to a low value of 0.54%. The TSMOR convergence plot is compared to the convergence of the LSPG approach with respect to the number of POD bases k of the snapshot matrix $\boldsymbol{M}$. Similar to Figure 12A, Figure 12B displays the relative errors in the LSPG solutions predicted at the same set of parameters for different numbers of bases. It can be observed that the error converges only to 5.24% even though all five POD bases were used for prediction. Hereafter, all the TSMOR predicted results presented for this problem are produced with nine Fourier modes.

Next, the performance of the proposed TSMOR approach is compared to several existing MOR techniques. Figure 13 illustrates the predictive capabilities of several MOR approaches for the parameter $\mu^* = 3.4$. The FOM density solution is shown in Figure 13A, whereas the new proposed TSMOR solution using two local bases corresponding to two nearby snapshots is shown in Figure 13B. Figure 13C corresponds to the solution obtained by LSPG using four POD modes of the snapshot matrix $\boldsymbol{M}$. Figure 13D corresponds to the L_1-dictionary approach using two local bases or dictionary elements. To compare these solutions qualitatively, the predicted density distributions at various y-locations for the FOM, TSMOR, LSPG, and L_1-dictionary approaches are shown in Figure 14. It can be observed that the proposed TSMOR approach significantly outperforms the LSPG and L_1-dictionary methods.

Finally, the relative solution error between the FOM solution and the predicted solution using the TSMOR, LSPG, and L_1-dictionary approaches across the entire parameter range of interest is given in Figure 15. For this case, predictions are made at two uniformly distributed parameters in every interval of μ_s. It can be observed that the solutions predicted using TSMOR have an average error of only 0.6% as compared to 5.9% in LSPG and 5.0% in the L_1-dictionary approach.

8.3 | Jet diffusion flame in a combustor

8.3.1 | Problem description

This problem consists of jets of fuel and oxidizer injected into a combustion chamber, as shown in Figure 16. The length (L) and height (H) of the chamber are 18 and 9 mm, respectively. The widths of fuel and oxidizer inlets are denoted as H_f and H_o, respectively. Inside the chamber, the fuel and oxidizer diffuse to form a diffusion flame where the combustion reaction is governed by an advection-diffusion–type governing equation, ie,

$$\nabla \cdot (\boldsymbol{W}\boldsymbol{w}(\boldsymbol{\mu})) - \nabla \cdot (\nu \nabla \boldsymbol{w}(\boldsymbol{\mu})) + \boldsymbol{F}(\boldsymbol{w}(\boldsymbol{\mu})) = 0 \qquad x \in [0, L], \quad y \in [0, H], \tag{35}$$

where the state variable $\boldsymbol{w}(\boldsymbol{\mu})$ represents the concentration of fuel in the chamber, $\boldsymbol{W} = W_x \hat{i} + W_y \hat{j}$ is the velocity field, and ν is the diffusion coefficient. The nonlinear reaction term $\boldsymbol{F}(\boldsymbol{w}(\boldsymbol{\mu}))$ is of Arrhenius type given by

$$\boldsymbol{F}(\boldsymbol{w}(\boldsymbol{\mu})) = A\boldsymbol{w}(\boldsymbol{\mu})(c - \boldsymbol{w}(\boldsymbol{\mu}))e^{-E/(d - \boldsymbol{w}(\boldsymbol{\mu}))}, \tag{36}$$
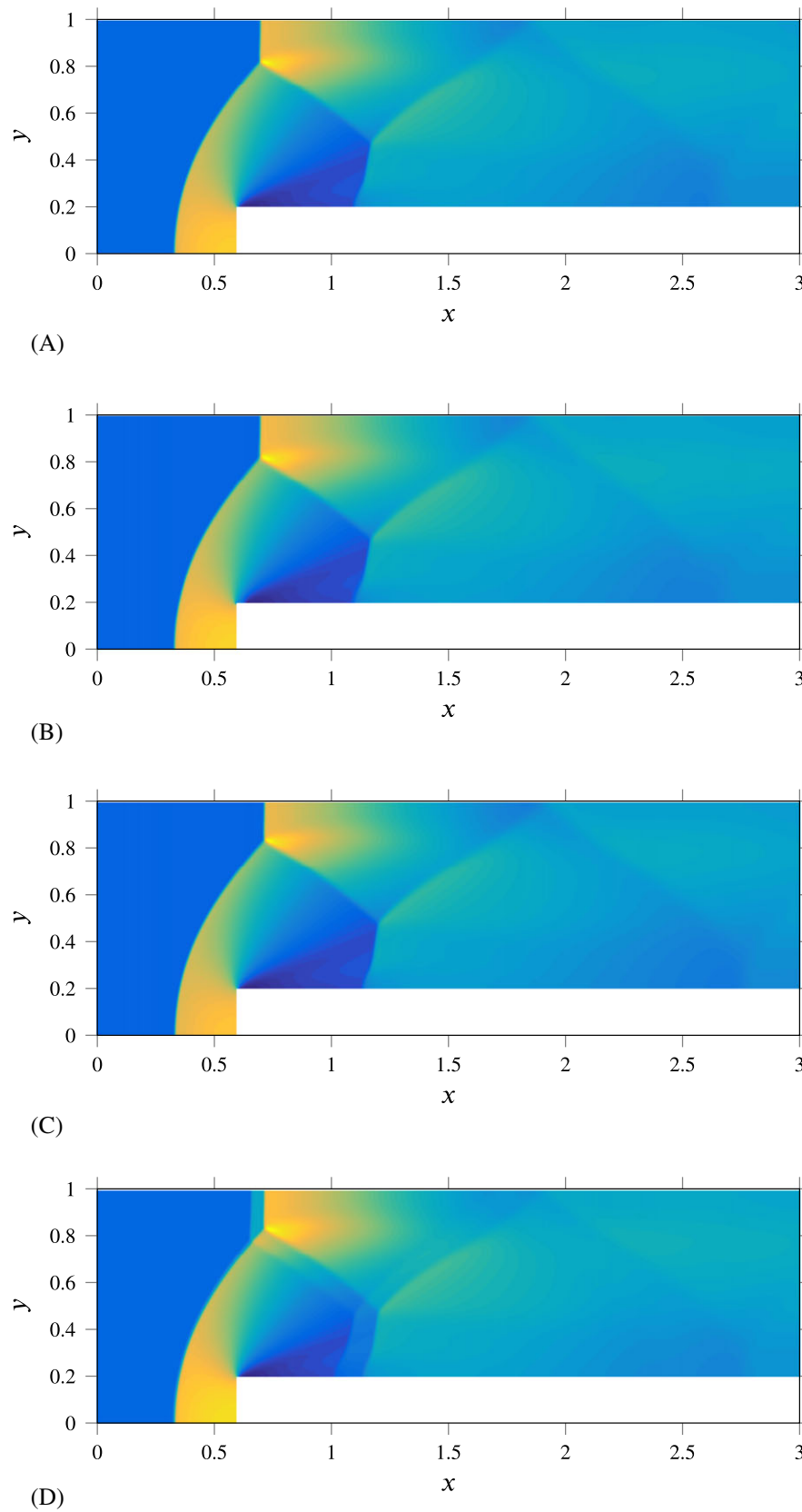
FIGURE 13 Comparison of steady-state density solutions at $\mu^* = 3.4$ predicted by the transported snapshot model order reduction (TSMOR), least squares Petrov-Galerkin (LSPG), and L_1-dictionary approaches with the full-order model (FOM) solution. A, FOM solution; B, TSMOR solution; C, LSPG solution; D, L_1-dictionary solution [Colour figure can be viewed at wileyonlinelibrary.com]
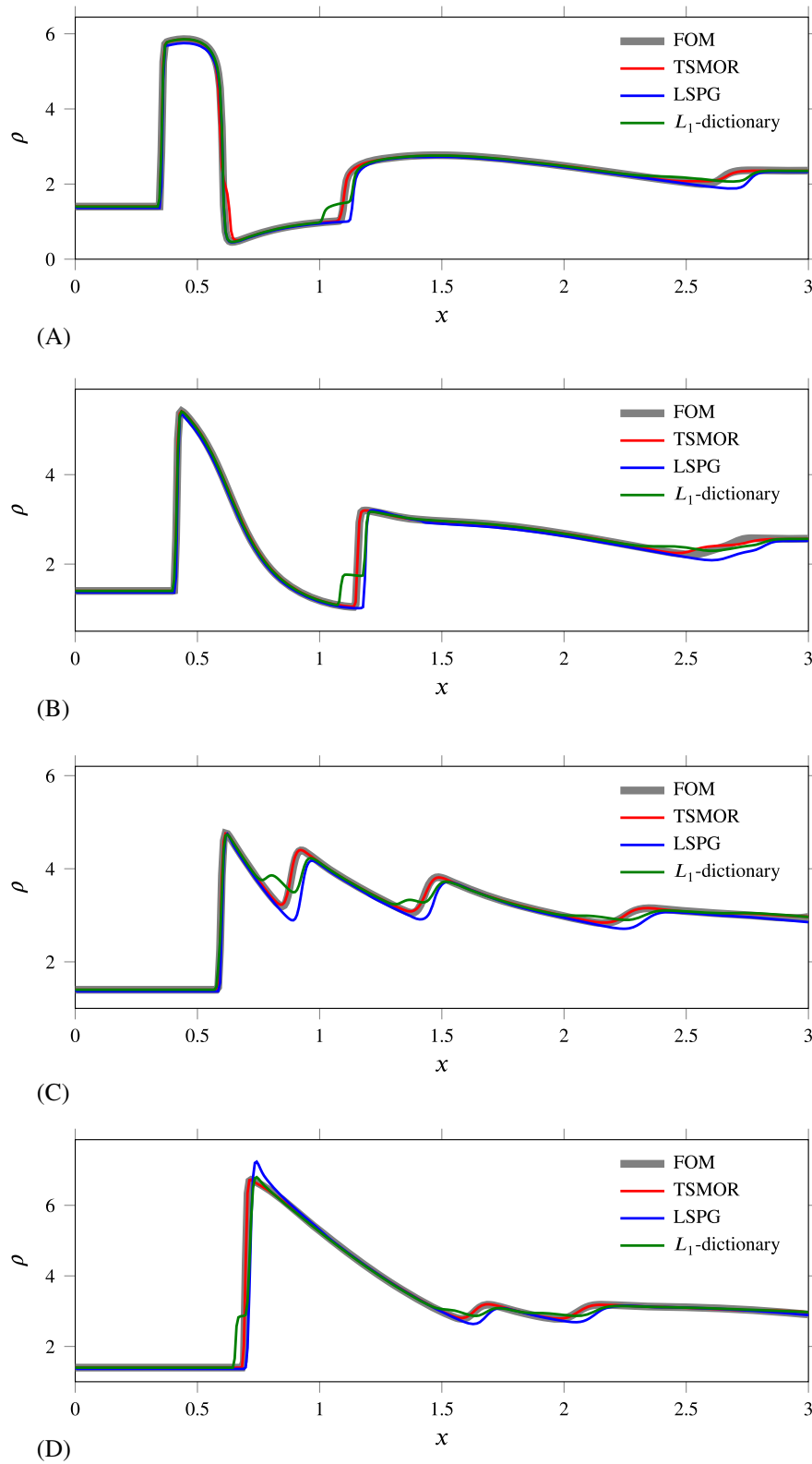
FIGURE 14 One-dimensional density plots of solutions predicted by the full-order model (FOM), transported snapshot model order reduction (TSMOR), least squares Petrov-Galerkin (LSPG), and L_1-dictionary approaches at various y-locations. A, $y = 0.205$; B, $y = 0.4$; C, $y = 0.7$; D, $y = 0.83$
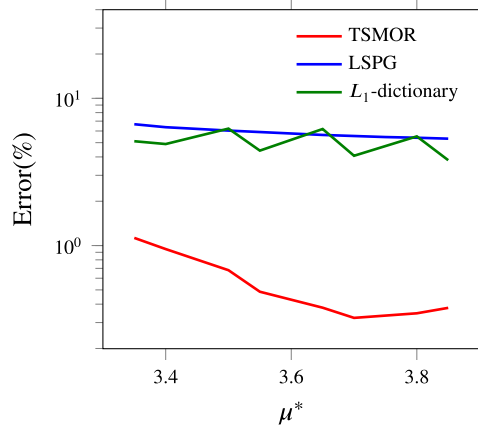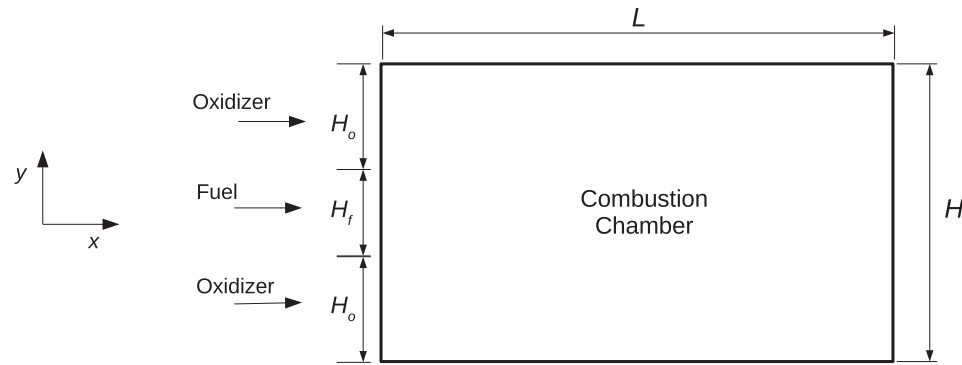
FIGURE 15 Performance comparison between the transported snapshot model order reduction (TSMOR), least squares Petrov-Galerkin (LSPG), and L_1-dictionary approaches for solution predictions at various parameters

FIGURE 16 Schematic of the combustion chamber

where c, d, A, and E are constants and $(c - \boldsymbol{w}(\boldsymbol{\mu}))$ represents the oxidizer concentration. The Dirichlet boundary condition is prescribed at the inlet, as follows:

$$\boldsymbol{w}(0, y; \boldsymbol{\mu}) = 0 \qquad y \in [0, H_o)$$
$$\boldsymbol{w}(0, y; \boldsymbol{\mu}) = c \qquad y \in [H_o, H_o + H_f]$$
$$\boldsymbol{w}(0, y; \boldsymbol{\mu}) = 0 \qquad y \in (H_o + H_f, H],$$

whereas homogeneous Neumann boundary conditions are prescribed on other boundaries.

In this problem, we consider parameter variations in three dimensions, where $\boldsymbol{\mu} = [W_y, ln(A), r]$ consists of the velocity field in the y-direction W_y, Arrhenius parameter $ln(A)$, and ratio of fuel-to-oxidizer inlet widths $r = H_f/H_o$. Moreover, W_y, $ln(A)$, and r influence the direction, length, and width of the flame, respectively. The values of the remaining constants are as follows: $W_x = 0.17$ m/s, $v = 5 \times 10^{-6}$ m^2/s, $c = 0.2$, $d = 0.24$, and $E = 0.1091$. The equations are discretized in space using a second-order, central finite difference scheme on a uniform Cartesian grid that is divided into 1 million grid points with $\Delta x = \Delta y = 10^{-5}$ mm. A fine discretization is chosen to demonstrate the speedup associated with the hyper-reduction approach. The resulting equations are solved using Newton's method until convergence of 10 orders of magnitude. Figure 17 shows the fuel concentration contours computed at eight different corners of the 3D parameter space. Clear and distinct flame fronts having different directions, lengths, and widths can be observed in these plots.

8.3.2 | Implementation of TSMOR

A snapshot matrix $\boldsymbol{M}$ containing 48 snapshots is generated on a $4 \times 4 \times 3$ grid in parameter space $\mathcal{D}$ at parameters $W_y \times ln(A) \times r \equiv [-0.02, 0, 0.02, 0.04] \times [7.0, 7.2, 7.4, 7.6] \times [0.467, 0.846, 1.364]$. The coefficients of the polynomial expansion (17) $\boldsymbol{c}^s$ for each snapshot are computed off-line by solving the training error minimization (23). Since the parameter W_y changes the angle of the flame, a strong coupling between the x and y coordinates is required. As a result, the bases of the polynomial expansion, $f_{x_p}(x, y)$ and $f_{y_p}(x, y)$, for the x and y transport fields, $c_{s_x}(x, y; \boldsymbol{\Delta\mu})$ and $c_{s_y}(x, y; \boldsymbol{\Delta\mu})$,
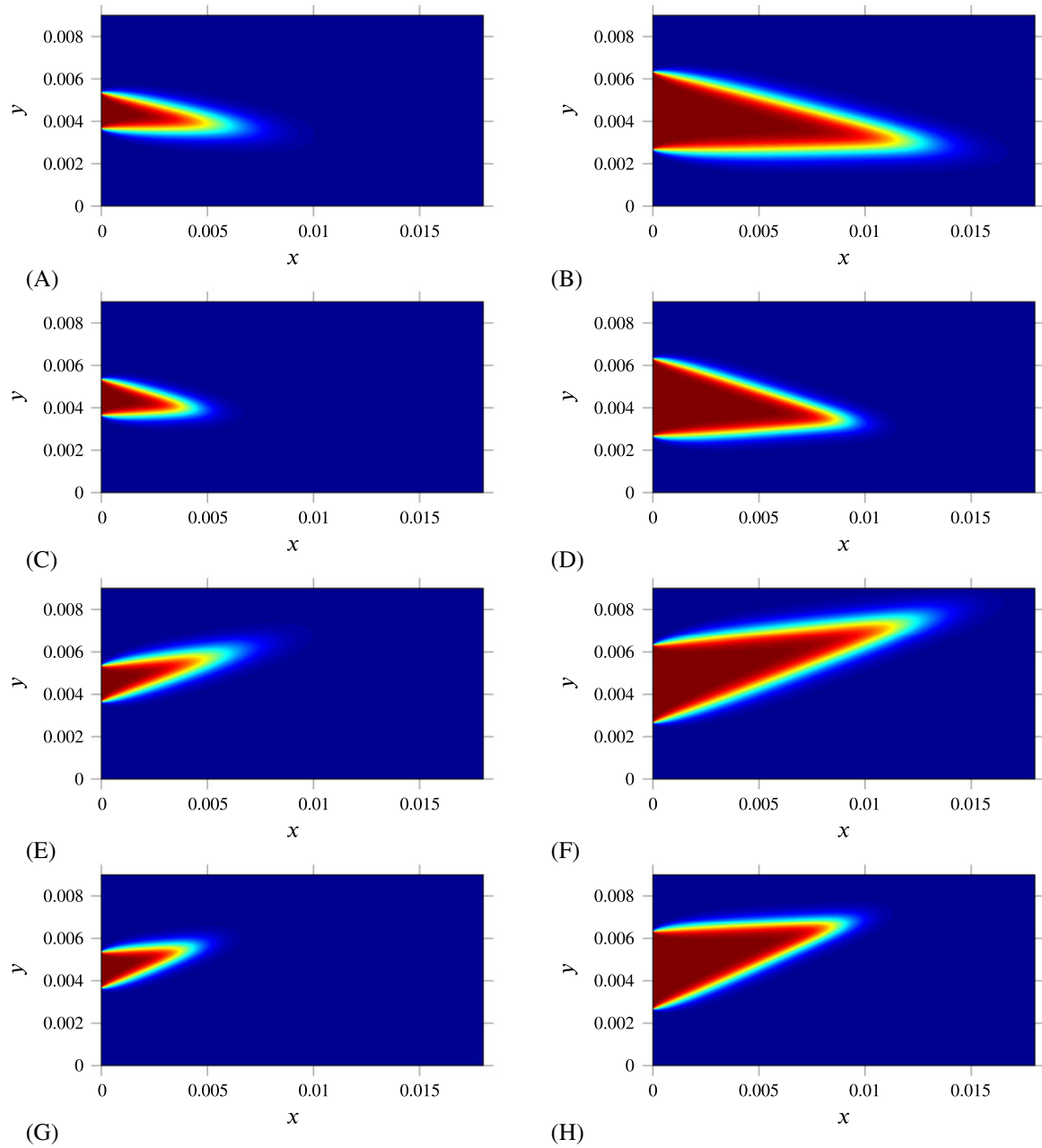
FIGURE 17 Fuel concentration $w(\mu)$ contours computed at eight different corners of the three-dimensional parameter space $\mathcal{D}$. A, $\mu = [-0.02, 7, 0.467]$; B, $\mu = [-0.02, 7, 1.364]$; C, $\mu = [-0.02, 7.6, 0.467]$; D, $\mu = [-0.02, 7.6, 1.364]$; E, $\mu = [0.04, 7, 0.467]$; F, $\mu = [0.04, 7, 1.364]$; G, $\mu = [0.04, 7.6, 0.467]$; H, Contour plot at $\mu = [0.04, 7.6, 1.364]$ [Colour figure can be viewed at wileyonlinelibrary.com]

respectively, are chosen to be a combination of coupled and decoupled Fourier sine series with m modes. Here, we take $f_{x_p}(x, y) = f_{y_p}(x, y) = f_p(x, y)$:

$$
\begin{aligned}
m = 1 \quad & \boldsymbol{f}(x, y) = \sin\left(\frac{\pi x}{2L}\right) \\
m = 2 \quad & \boldsymbol{f}(x, y) = \left[\boldsymbol{f}(x, y)\big|_{m=1}, \sin\left(\frac{\pi x}{L}\right), \sin\left(\frac{\pi y}{H}\right)\right] \\
m = 3 \quad & \boldsymbol{f}(x, y) = \left[\boldsymbol{f}(x, y)\big|_{m=2}, \sin\left(\frac{2\pi x}{L}\right), \sin\left(\frac{\pi x}{L}\right)\sin\left(\frac{\pi y}{H}\right), \sin\left(\frac{2\pi y}{H}\right)\right] \\
m = 4 \quad & \boldsymbol{f}(x, y) = \left[\boldsymbol{f}(x, y)\big|_{m=3}, \sin\left(\frac{3\pi x}{L}\right), \sin\left(\frac{2\pi x}{L}\right)\sin\left(\frac{\pi y}{H}\right), \sin\left(\frac{\pi x}{L}\right)\sin\left(\frac{2\pi y}{H}\right), \sin\left(\frac{3\pi y}{H}\right)\right].
\end{aligned}
\tag{37}
$$

Note that the basis functions in Equation (37) are cumulative in the sense that for $m > 1$, the basis includes the basis corresponding to the previous modes as well. Since the inlet boundary condition for this problem is discontinuous, boundary conditions on the transported snapshots are enforced by enforcing appropriate conditions on the transports, as described in Remark 6 of Section 5. More specifically, to avoid extrapolation in the x-direction, the following condition is imposed on the x-transports at the inlet: $c_{s_x}(x = 0, y; \Delta\mu) = 0$. This condition is enforced by setting the coefficients of decoupled basis $\sin(i\pi y/H) = 0$ for $i = 1, 2, 3$ in the expansion of $c_{s_x}(x, y; \Delta\mu)$. Note that this condition is not enforced on y-transports $c_{s_y}(x, y; \Delta\mu)$. For this multidimensional parameter problem, $g_q(\Delta\mu)$ is given by

$$g(\Delta\mu) = [\Delta\mu_1, \ \Delta\mu_2, \ \Delta\mu_3, \ \Delta\mu_1\Delta\mu_2, \ \Delta\mu_2\Delta\mu_3, \ \Delta\mu_3\Delta\mu_1, \ \Delta\mu_1\Delta\mu_2\Delta\mu_3]. \tag{38}$$

Transformation of the structured Cartesian grid on the basis of the coupled transports (37) leads to a nontensor grid. Hence, interpolation from the nontensor transported grid to the original grid must be performed using the `scatteredInterpolant` algorithm in MATLAB. Unfortunately, this interpolation scheme is computationally prohibitive for large grids. Therefore, during the off-line stage, the snapshots are uniformly downsampled by a factor Δs in the x and y coordinates, leading to a coarser grid with $N_{\Delta s}$ points. A grid convergence study is conducted to identify Δs and $N_{\Delta s}$. Figure 18 plots the relative error in the TSMOR solutions predicted at $\mu^* = [-0.01, 7.1, 0.644]$ for increasing $N_{\Delta s}$. It can be observed that the reduction in error is minimal after 3000 grid points, which corresponds to a downsampling factor of 25. Hence, the snapshots are uniformly downsampled by a factor of 25. Note that this downsampling process is conducted *only* during the off-line stage.
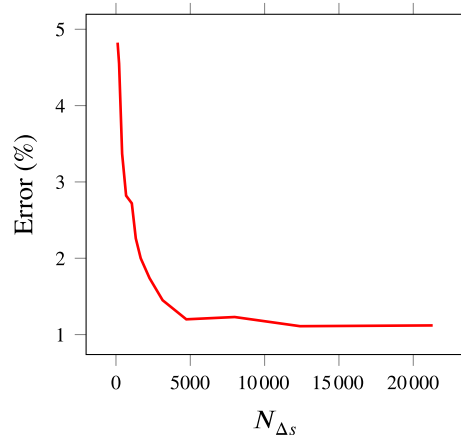

FIGURE 18 Grid convergence study for the off-line stage of the proposed transported snapshot model order reduction approach [Colour figure can be viewed at wileyonlinelibrary.com]
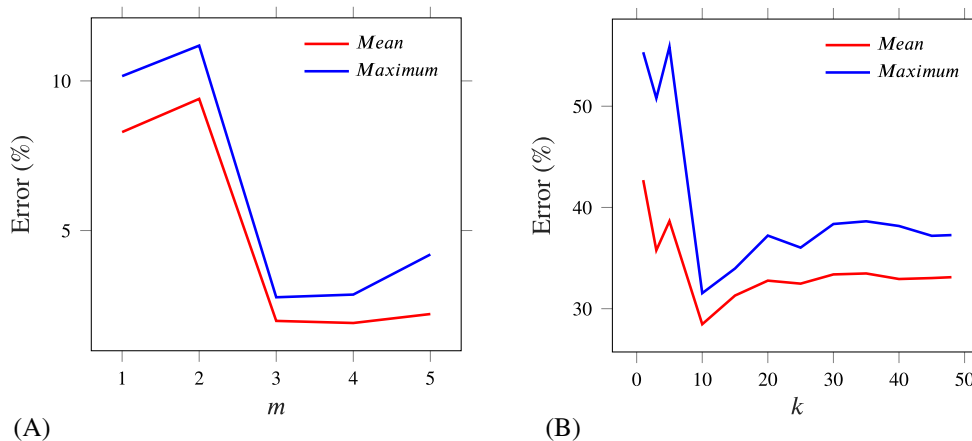

FIGURE 19 Convergence plot of the relative error for transported snapshot model order reduction (TSMOR) and least squares Petrov-Galerkin (LSPG) predicted solutions. A, Plot of relative error vs number of Fourier modes m for TSMOR predicted solutions; B, Plot of relative error vs number of proper orthogonal decomposition bases k for LSPG predicted solutions

Next, convergence of the proposed TSMOR approach with respect to the number of Fourier modes m is studied by predicting new solutions in the predictive regime μ^*. Figure 19A shows the mean and maximum relative errors in the TSMOR solutions predicted at 18 uniformly distributed parameters in the parameter space $\mathcal{D}$ for different numbers of Fourier modes m. It can be observed that as the number of Fourier modes increases, the error converges to a low value of 1.91%. The TSMOR convergence plot is compared to the convergence of the LSPG approach with respect to the number of POD bases k of the snapshot matrix $\boldsymbol{M}$. Similar to Figure 19A, Figure 19B displays the relative errors in the LSPG solutions predicted at the same set of parameters for different numbers of bases. It can be observed that the error converges only to 30% even though all 48 POD bases were used for prediction. Hereafter, all the TSMOR predicted results presented for this problem are produced with four Fourier modes.

Next, the TSMOR approach is equipped with the hyper-reduction strategy mentioned in Section 6. First, 70 collocation points are obtained by using the DEIM algorithm. Second, these points are augmented with 30 uniformly distributed inlet points. Finally, an additional $\hat{n}_w \approx n_w \times 4 = 400$ points $\hat{\varepsilon}$ are included to enable the evaluation of the residuals via the central finite difference scheme.

To demonstrate the performance of the proposed TSMOR approach, solutions are predicted at four different predictive regimes in the parameter space $\mathcal{D}$ and compared with the FOM and several other MOR techniques. Parameters corresponding to these test cases are tabulated in Table 1. Figures 20-23 illustrate the predictive capabilities of several MOR approaches for these test cases. Contour plots at contour levels $\boldsymbol{w}(\boldsymbol{\mu}^*) = 0.018$ and $\boldsymbol{w}(\boldsymbol{\mu}^*) = 0.15$ are displayed in these

TABLE 1 Table of four predictive test cases

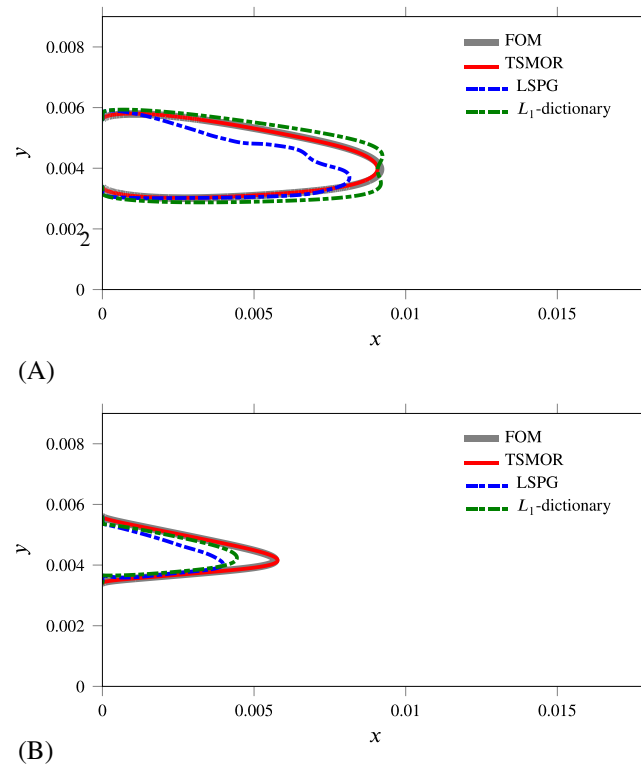| μ^*	$\mu_1^* \equiv W_y$	$\mu_2^* \equiv ln(A)$	$\mu_3^* \equiv r$
Case 1	−0.01	7.1	0.643
Case 2	0.005	7.3	1.083
Case 3	0.015	7.35	0.643
Case 4	0.025	7.5	1.083

FIGURE 20 Case 1: comparison of predicted solutions at $\boldsymbol{\mu}^* = [−0.01, 7.1, 0.643]$ using transported snapshot model order reduction (TSMOR), least squares Petrov-Galerkin (LSPG), and the L_1-dictionary approach with the full-order model (FOM). A, Contour plot for $\boldsymbol{w}(\boldsymbol{\mu}^*) = 0.018$; B, Contour plot for $\boldsymbol{w}(\boldsymbol{\mu}^*) = 0.15$
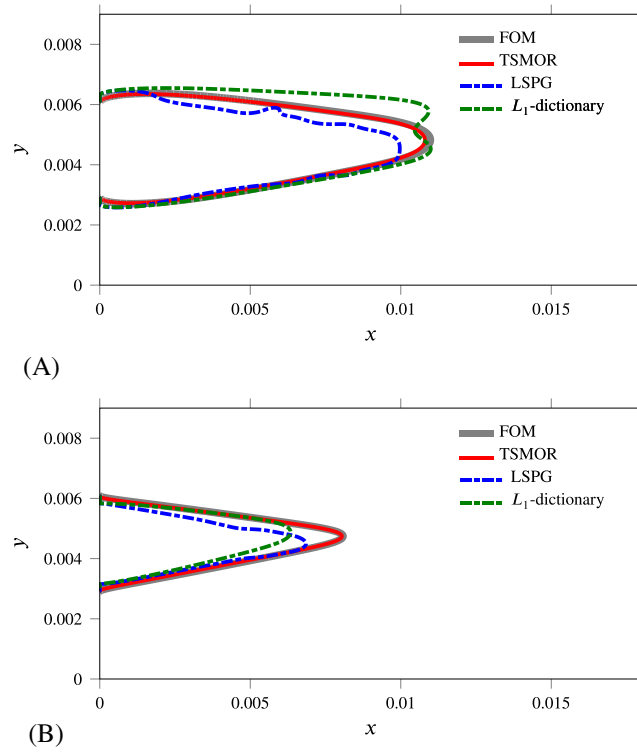
FIGURE 21 Case 2: comparison of predicted solutions at $\mu^* = [0.005, 7.3, 1.083]$ using transported snapshot model order reduction (TSMOR), least squares Petrov-Galerkin (LSPG), and the L_1-dictionary approach with the full-order model (FOM). A, Contour plot for $w(\mu^*) = 0.018$; B, Contour plot for $w(\mu^*) = 0.15$
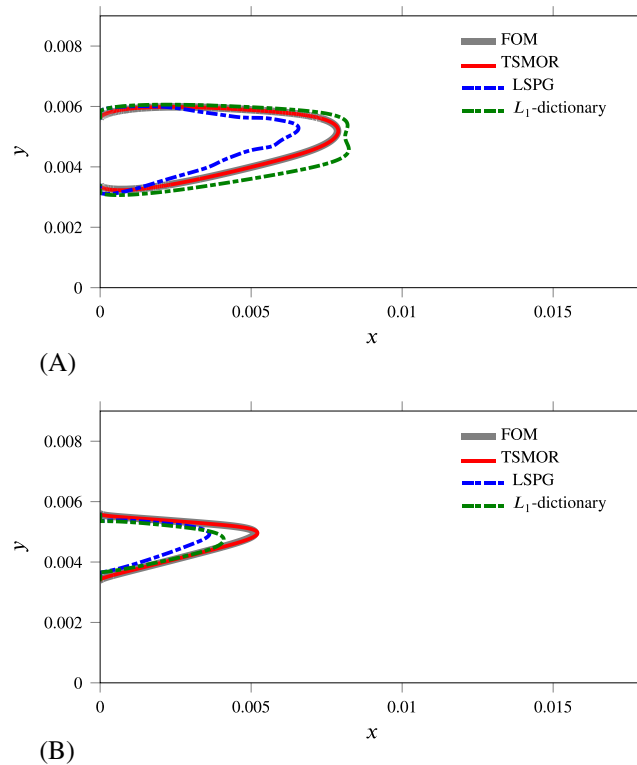

FIGURE 22 Case 3: comparison of predicted solutions at $\mu^* = [0.015, 7.35, 0.643]$ using transported snapshot model order reduction (TSMOR), least squares Petrov-Galerkin (LSPG), and the L_1-dictionary approach with the full-order model (FOM). A, Contour plot for $w(\mu^*) = 0.018$; B, Contour plot for $w(\mu^*) = 0.15$
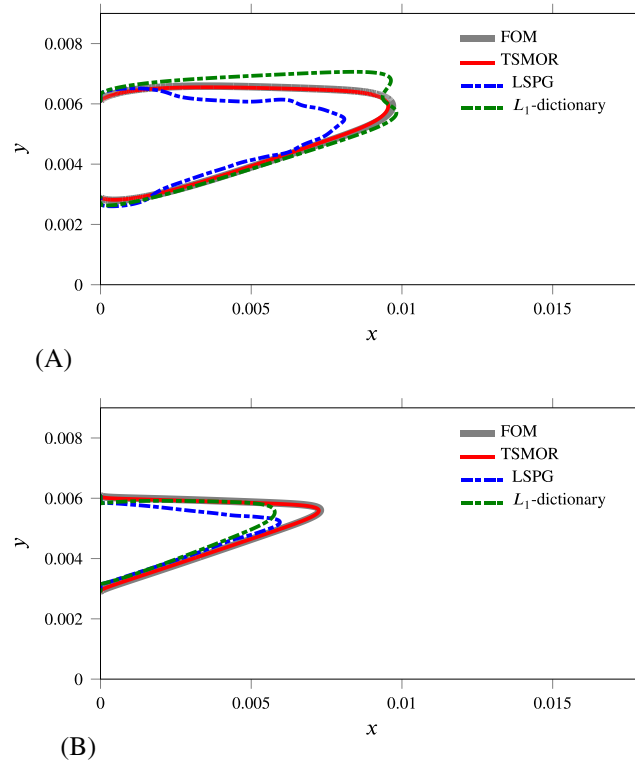
FIGURE 23 Case 4: comparison of predicted solutions at $\mu^* = [0.025, 7.5, 1.083]$ using transported snapshot model order reduction (TSMOR), least squares Petrov-Galerkin (LSPG), and the L_1-dictionary approach with the full-order model (FOM). A, Contour plot for $w(\mu^*) = 0.018$; B, Contour plot for $w(\mu^*) = 0.15$

figures. The FOM is given by the gray lines, whereas the new proposed TSMOR+HR approach using eight local bases is given by the red lines. The blue lines correspond to the solution obtained by LSPG using 48 POD modes of the snapshot matrix $\mathbf{M}$. The green lines correspond to the L_1-dictionary approach using eight local bases or dictionary elements. The proposed TSMOR approach predicts a solution that accurately matches the FOM solutions in all the four cases. In contrast, both the LSPG and L_1-dictionary methods fail to capture the flame front.

The ROM errors for the various MOR approaches are summarized in Table 2. Solutions predicted using TSMOR have an average error of only 1.92% as compared to 29.02% in LSPG and 17.53% in the L_1-dictionary approach. The Table also provides the error in the POD-projected solution, which is obtained by projecting the FOM onto 48 POD bases of the snapshot matrix $\mathbf{M}$. The average error for the POD-projected solution is 8.65%. Thus, TSMOR significantly outperforms the LSPG and L_1-dictionary approaches, and it is three to four times better than the POD-projected solutions.

Finally, wall times and speedups for the FOM and the online stage of TSMOR+HR are given in Table 3. Here, speedup is defined as the ratio of wall times of the FOM to the online stage of TSMOR+HR. TSMOR+HR delivers a speedup of two orders of magnitude.

TABLE 2 Comparison of relative error (%) in the predicted solution at μ^* for four different cases

Model	TSMOR+HR (8 Local Bases)	POD Projection (48 Global Bases)	LSPG (48 Global Bases)	L_1-Dictionary (8 Local Bases)
Case 1	1.07	9.12	27.34	15.49
Case 2	2.47	8.43	23.95	18.54
Case 3	1.24	8.72	32.74	18.25
Case 4	2.92	8.32	32.07	17.83

Abbreviations: LSPG, least squares Petrov-Galerkin; POD, proper orthogonal decomposition; TSMOR+HR, hyper-reduced transported snapshot model order reduction.

TABLE 3 Central processing unit wall times associated with the full-order model (FOM) and the online stage of hyper-reduced transported snapshot model order reduction (TSMOR+HR) for the prediction at $\boldsymbol{\mu}^*$ for four different cases

Model	FOM (s)	TSMOR+HR (s)	Speedup
Case 1	169.01	0.43	393
Case 2	202.37	0.46	440
Case 3	166.05	0.63	263
Case 4	208.23	0.71	293

9 | LIMITATIONS OF TSMOR

TSMOR can be expected to provide significant improvements in accuracy over traditional projection-based ROMs for a large class of problems characterized by shocks and sharp gradients whose spatial locations and orientations are strongly parameter dependent. There are, however, a large class of important and very challenging problems where TSMOR—and, indeed, most other related methodologies in the literature—can be expected to fail.

For example, similar to most other model reduction approaches for parameter variations in the literature, TSMOR requires that the topology of the underlying solution varies smoothly with respect to the parameters. In other words, TSMOR cannot be expected to provide accurate predictions of bifurcations. In the case when the changes in solutions with respect to parameter variations are sharp yet still smooth and continuous, an adaptive parameter sampling[13] strategy during the off-line stage can be expected to mitigate this issue.

Finally, since both the online and off-line stages of TSMOR require solutions of nonconvex optimization problems (Equations (22) and (23), respectively), convergence to local, suboptimal minima can be a real problem. However, in principle, this issue can usually be avoided by implementing a global optimization scheme or, more typically, refining and/or adaptively sampling the parameter space during the off-line stage.

10 | CONCLUSIONS

In this paper, a TSMOR method for predicting new parametric steady-state solutions containing moving shocks and discontinuities has been presented. In this method, the solution is approximated by a linear combination of spatially transported snapshots. The transports are assumed to be smooth in parameter as well as physical space and, hence, approximated as a low-order polynomial expansion. The coefficients of the polynomial expansion are obtained by solving a training error minimization problem at the off-line stage. The generalized coordinates are derived by solving a residual minimization problem at the online stage. TSMOR is also integrated with hyper-reduction methods to reduce the computational complexity of evaluating the nonlinear residual and parameter-dependent basis at the online stage.

Numerical experiments consist of a 1D converging-diverging nozzle problem with the throat area as the parameter, a supersonic flow over a forward-facing step with the inlet Mach number as the parameter, and a multidimensional parametric combustion problem with three parameters influencing the length, direction, and width of the diffusion flame. For all parameters considered, TSMOR is demonstrated to significantly outperform traditional approaches such as those based on linear compression schemes, eg, LSPG and more recent local basis approaches such as L_1-dictionary. Furthermore, speedups of two and four orders of magnitude for the combustion and nozzle problems are achieved, respectively.

ORCID

Nirmal J. Nair https://orcid.org/0000-0003-4431-4020

REFERENCES

1. Galletti B, Bruneau CH, Zannetti L, Iollo A. Low-order modelling of laminar flow regimes past a confined square cylinder. *J Fluid Mech*. 2004;503:161-170.

2. Holmes P, Lumley JL, Berkooz G, Rowley CW. *Turbulence, Coherent Structures, Dynamical Systems and Symmetry*. 2nd ed. Cambridge, UK: Cambridge University Press; 2012.

3. Rowley CW, Mezić I, Bagheri S, Schlatter P, Henningson DS. Spectral analysis of nonlinear flows. *J Fluid Mech*. 2009;641:115-127.

4. Schmid PJ. Dynamic mode decomposition of numerical and experimental data. *J Fluid Mech*. 2010;656:5-28.

5. Rowley CW. Model reduction for fluids, using balanced proper orthogonal decomposition. *Int J Bifurc Chaos*. 2005;15(3):997-1013.

6. Willcox K, Peraire J. Balanced model reduction via the proper orthogonal decomposition. *AIAA J*. 2002;40(11):2323-2330.

7. Gugercin S, Antoulas AC. A survey of model reduction by balanced truncation and some new results. *Int J Control*. 2004;77(8):748-766.

8. Moore B. Principal component analysis in linear systems: controllability, observability, and model reduction. *IEEE Trans Autom Control*. 1981;26(1):17-32.

9. Rozza G. Reduced basis approximation and error bounds for potential flows in parametrized geometries. *Commun Comput Phys*. 2011;9(1):1-48.

10. Veroy K, Patera AT. Certified real-time solution of the parametrized steady incompressible Navier-Stokes equations: rigorous reduced-basis *a posteriori* error bounds. *Int J Numer Methods Fluids*. 2005;47(8-9):773-788.

11. Benner P, Gugercin S, Willcox K. A survey of projection-based model reduction methods for parametric dynamical systems. *SIAM Rev*. 2015;57(4):483-531.

12. Iman RL. Latin hypercube sampling. Wiley StatsRef: Statistics Reference Online. 2014. https://doi:10.1002/9781118445112.stat03803

13. Paul-Dubois-Taine A, Amsallem D. An adaptive and efficient greedy procedure for the optimal training of parametric reduced-order models. *Int J Numer Methods Eng*. 2015;102(5):1262-1292.

14. Rozza G, Huynh DBP, Patera AT. Reduced basis approximation and a posteriori error estimation for affinely parametrized elliptic coercive partial differential equations. *Arch Comput Methods Eng*. 2008;15(3):229.

15. Bui-Thanh T, Willcox K, Ghattas O. Parametric reduced-order models for probabilistic analysis of unsteady aerodynamic applications. *AIAA J*. 2008;46(10):2520-2529.

16. Bui-Thanh T, Willcox K, Ghattas O. Model reduction for large-scale systems with high-dimensional parametric input space. *SIAM J Sci Comput*. 2008;30(6):3270-3288.

17. Rewieński M, White J. Model order reduction for nonlinear dynamical systems based on trajectory piecewise-linear approximations. *Linear Algebra Appl*. 2006;415(2-3):426-454.

18. Lieu T, Farhat C, Lesoinne M. Reduced-order fluid/structure modeling of a complete aircraft configuration. *Comput Methods Appl Mech Eng*. 2006;195(41-43):5730-5742.

19. Amsallem D, Cortial J, Farhat C. Toward real-time computational-fluid-dynamics-based aeroelastic computations using a database of reduced-order information. *AIAA J*. 2010;48(9):2029-2037.

20. Carlberg K, Bou-Mosleh C, Farhat C. Efficient non-linear model reduction via a least-squares Petrov-Galerkin projection and compressive tensor approximations. *Int J Numer Methods Eng*. 2011;86(2):155-181.

21. Yano M, Patera AT, Urban K. A space-time hp-interpolation-based certified reduced basis method for Burgers' equation. *Math Models Methods Appl Sci*. 2014;24(9):1903-1935.

22. Dahmen W. How to best sample a solution manifold? In: *Sampling Theory, A Renaissance: Compressive Sensing and Other Developments*. Cham, Switzerland: Springer International Publishing Switzerland; 2015:403-435.

23. Washabaugh K, Amsallem D, Zahr M, Farhat C. Nonlinear model reduction for CFD problems using local reduced-order bases. Paper presented at: 42nd AIAA Fluid Dynamics Conference and Exhibit; 2012; New Orleans, LA.

24. Amsallem D, Zahr MJ, Farhat C. Nonlinear model order reduction based on local reduced-order bases. *Int J Numer Methods Eng*. 2012;92(10):891-916.

25. Zahr MJ, Amsallem D, Farhat C. Construction of parametrically-robust CFD-based reduced-order models for PDE-constrained optimization. Paper presented at: 21st AIAA Computational Fluid Dynamics Conference; 2013; San Diego, CA.

26. Amsallem D, Farhat C. An online method for interpolating linear parametric reduced-order models. *SIAM J Sci Comput*. 2011;33(5):2169-2198.

27. Amsallem D, Cortial J, Carlberg K, Farhat C. A method for interpolating on manifolds structural dynamics reduced-order models. *Int J Numer Methods Eng*. 2009;80(9):1241-1258.

28. Bui-Thanh T, Damodaran M, Willcox K. Proper orthogonal decomposition extensions for parametric applications in compressible aerodynamics. Paper presented at: 21st AIAA Applied Aerodynamics Conference; 2003; Orlando, FL.

29. Franz T, Zimmermann R, Görtz S, Karcher N. Interpolation-based reduced-order modelling for steady transonic flows via manifold learning. *Int J Comput Fluid Dyn*. 2014;28(3-4):106-121.

30. Hummel T, Temmler C, Schuermans B, Sattelmayer T. Reduced-order modeling of aeroacoustic systems for stability analyses of thermoacoustically noncompact gas turbine combustors. *J Eng Gas Turbines Power*. 2016;138(5):051502.

31. Balajewicz M, Farhat C. Reduction of nonlinear embedded boundary models for problems with evolving interfaces. *J Comput Phys*. 2014;274:489-504.

32. Balajewicz M, Toivanen J. Reduced order models for pricing American options under stochastic volatility and jump-diffusion models. *Procedia Comput Sci*. 2016;80:734-743.

33. Washabaugh K, Zahr MJ, Farhat C. On the use of discrete nonlinear reduced-order models for the prediction of steady-state flows past parametrically deformed complex geometries. Paper presented at: 54th AIAA Aerospace Sciences Meeting; 2016; San Diego, CA.

34. Rim D, Moe S, LeVeque RJ. Transport reversal for model reduction of hyperbolic partial differential equations. *SIAM/ASA J Uncertainty Quantification*. 2018;6(1):118-150.

35. Mowlavi S, Sapsis TP. Model order reduction for stochastic dynamical systems with continuous symmetries. *SIAM J Sci Comput*. 2018;40(3):A1669-A1695.

36. Rowley CW, Marsden JE. Reconstruction equations and the Karhunen-Loève expansion for systems with symmetry. *Phys D Nonlinear Phenom*. 2000;142(1-2):1-19.

37. Iollo A, Lombardi D. Advection modes by optimal mass transfer. *Phys Rev E*. 2014;89(2):022923.

38. Carlberg K. Adaptive *h*-refinement for reduced-order models. *Int J Numer Methods Eng*. 2015;102(5):1192-1210.

39. Welper G. Interpolation of functions with parameter dependent jumps by transformed snapshots. *SIAM J Sci Comput*. 2017;39(4):A1225-A1250.

40. Reiss J, Schulze P, Sesterhenn J, Mehrmann V. The shifted proper orthogonal decomposition: a mode decomposition for multiple transport phenomena. *SIAM J Sci Comput*. 2018;40(3):A1322-A1344.

41. Cagniart N, Maday Y, Stamm B. Model order reduction for problems with large convection effects. Preprint hal-01395571. 2016.

42. Mojgani R, Balajewicz M. Lagrangian basis method for dimensionality reduction of convection dominated nonlinear flows. Preprint arXiv. 1701.04343. 2017.

43. Ohlberger M, Rave S. Nonlinear reduced basis approximation of parameterized evolution equations via the method of freezing. *Comptes Rendus Math*. 2013;351(23-24):901-906.

44. Lucia DJ, King PI, Oxley ME, Beran PS. Reduced order modeling for a one-dimensional nozzle flow with moving shocks. Paper presented at: 15th AIAA Computational Fluid Dynamics Conference; 2001; Anaheim, CA.

45. Constantine PG, Iaccarino G. Reduced order models for parameterized hyperbolic conservations laws with shock reconstruction. Stanford, CA: Center for Turbulence Research, Stanford University; 2012. Annual research briefs.

46. Cagniart N, Crisovan R, Maday Y, Abgrall R. Model order reduction for hyperbolic problems: a new framework. Preprint hal-01583224. 2017.

47. Chaturantabut S, Sorensen DC. Nonlinear model reduction via discrete empirical interpolation. *SIAM J Sci Comput*. 2010;32(5):2737-2764.

48. Carlberg K, Cortial J, Amsallem D, Zahr M, Farhat C. The GNAT nonlinear model reduction method and its application to fluid dynamics problems. Paper presented at: 6th AIAA Theoretical Fluid Mechanics Conference; 2011; Honolulu, HI.

49. Farhat C, Avery P, Chapman T, Cortial J. Dimensional reduction of nonlinear finite element dynamic models with finite rotations and energy-based mesh sampling and weighting for computational efficiency. *Int J Numer Methods Eng*. 2014;98(9):625-662.

50. Abgrall R, Amsallem D, Crisovan R. Robust model reduction by L^1-norm minimization and approximation via dictionaries: application to nonlinear hyperbolic problems. *Adv Model Simul Eng Sci*. 2016;3(1):1.

51. Holland PW, Welsch RE. Robust regression using iteratively reweighted least-squares. *Commun Stat-Theory Methods*. 1977;6(9):813-827.

52. Daubechies I, DeVore R, Fornasier M, Güntürk CS. Iteratively reweighted least squares minimization for sparse recovery. *Commun Pure Appl Math*. 2010;63(1):1-38.

53. Carlberg K, Farhat C, Cortial J, Amsallem D. The GNAT method for nonlinear model reduction: effective implementation and application to computational fluid dynamics and turbulent flows. *J Comput Phys*. 2013;242:623-647.

54. Papadakis N. *Optimal Transport for Image Processing* [PhD thesis]. Bordeaux, France: Université de Bordeaux; 2015.

55. Iollo A, Lombardi D. A Lagrangian scheme for the solution of the optimal mass transfer problem. *J Comput Phys*. 2011;230(9):3430-3442.

56. Welper G. *h* and *hp*-adaptive interpolation by transformed snapshots for parametric and stochastic hyperbolic PDEs. Preprint arXiv. 1710.11481. 2017.

57. Galbally D, Fidkowski K, Willcox K, Ghattas O. Non-linear model reduction for uncertainty quantification in large-scale inverse problems. *Int J Numer Methods Eng*. 2010;81(12):1581-1608.

58. Woodward P, Colella P. The numerical simulation of two-dimensional fluid flow with strong shocks. *J Comput Phys*. 1984;54(1):115-173.

59. Gottlieb S. On high order strong stability preserving Runge-Kutta and multi step time discretizations. *J Sci Comput*. 2005;25(1-2):105-128.